Establishing Fluid Dynamics Scales Critical to Dynamic Interface Applications and their Impact on Handling Qualities

Quarterly Status Report 6

Period of Performance: 6/5/2022 – 9/4/2022

Prepared by:

G. R. Whitehouse
Continuum Dynamics, Inc.
34 Lexington Avenue
Ewing, NJ 08618-2302

Prepared for:

David Gonzalez
Office of Naval Research
875 North Randolph
Street
Arlington VA 22203

Under Contract No. N00014-21-C-1044

Glen R. Whitehouse

September 7, 2022

Project Summary

One of the most demanding tasks for naval aviators is landing on a moving flight deck in high sea-states (i.e. the dynamic interface (DI) problem - see Figure 1). This task is made even more difficult by aerodynamic disturbances at the landing spot from the flow around the ship's bow, superstructure and deck edges. This highly unsteady ship airwake can lead to significant pilot workload. Flight simulation has long been recognized as a valuable tool for augmenting engineering development and pilot training in DI operations, however, it is most effective when the underlying simulation model has appropriately characterized the complex aerodynamic interactions between the rotorcraft and ship airwake. Given the complexity of the problem, a fundamental difficulty when assessing the simulation approaches is the quantification of "good enough", both from the standpoint of understanding and predicting the underlying physics and also with regards to trainer fidelity (i.e. can the pilot feel/tell a difference). The premise of the proposed effort is to quantify "good enough" with regards to understanding the fundamental aero-physics of a rotorcraft interacting with an external disturbance field to quantify which length and time scales - such as those present in a ship airwake or in the wake of a an upstream aircraft during formation flight/refueling - directly impact the aircraft's fundamental response and flying qualities (FQ) along with the aeromechanics modeling fidelity required to simulate interactions adequately.

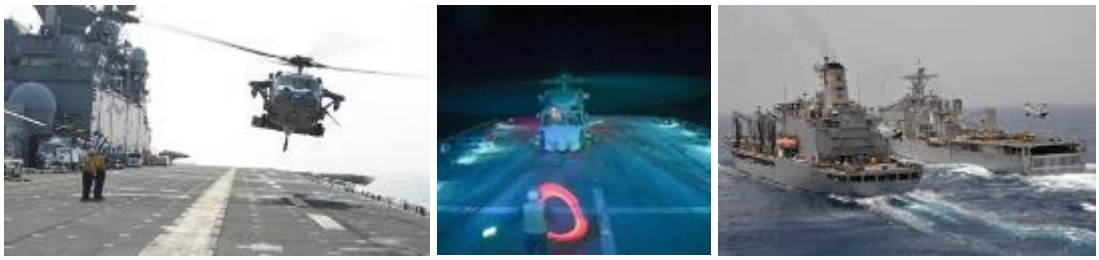

Figure 1: DI scenarios: landing on a moving deck (left), night operations (center) and approaching a pair ships (right)

Several ONR funded efforts that seek to quantify "good enough" have recently completed, or are underway, at the University of Maryland, Georgia Institute of Technology and NAVAIR, where the academic researchers are focusing on understanding the response of a wing to the wake shed by canonical structures [1] and the latter (Generalized Airwake Goodness Evaluation) program seeks to represent the entire DI scenario with a variety of methods. This effort does not seek to duplicate that work, rather to complement it by focusing on several fundamental unknowns in the rotorcraft community, namely:

1. What spatial and temporal scales, present in a disturbance field, matter from Flight Dynamics (FD) and FQ standpoints? Beyond the obvious constraints (i.e. larger than a rotor radius and those that induce velocities larger than the wake induced velocity), how does a rotor respond to different size disturbances and how does the rotor type influence this? For example, in general, a rotor acts to filter the influence of a disturbance field, but the level of filtering will vary significantly between an articulated flexible rotor (H-60) and a gimballed stiff one (V-22). Moreover, rotors typically respond ~90^o out of phase of the disturbance, whereas fixed aerodynamic surfaces response directly in-phase, which results in a fundamentally different response between rotorcraft types (i.e. helicopter vs. tiltrotor).

2. How do these scales vary when the effects on the full aircraft are accounted for? The primary response from the helicopter will be dominated by that of the rotor, though there may still be significant response associated with the disturbance induced flow on the fuselage, empennage and tail rotor.
3. How do these scales vary with aircraft configuration/type (i.e. conventional helicopter vs. tiltrotor)? The primary response from the helicopter will be dominated by that of the rotor, whereas the tiltrotor may respond primarily in a fixed wing manner associated with the induced flow on the wing. Of course, the tiltrotor's response will also vary with nacelle angle, and it is well known that the V-22's response to wake disturbances (i.e. during formation flight) is quite different to other rotorcraft in the Navy's inventory [2].
4. How do these scales vary with aircraft flight condition, and can valid modeling simplifications be made (i.e. distorting vs. classical frozen disturbance field)? Work by Whitehouse and Brown for helicopter rotors [3-7] suggests that for high speed flight, the traditional frozen field (superposition) assumption may be adequate, but that at the low speeds associated with DI operations, a distorting disturbance field and wake are required because the response is critically different.

Developing an understanding of fundamental aircraft aeromechanic response, FD, and FQ to the unknowns outlined above would provide great utility to the community with regards to establishing the level of modeling fidelity required to accurately simulate disturbance interactions, the level of fidelity required to be output by CFD simulation generated ship airwake databases for training scenarios, and the quantification and specification of handling qualities to types of disturbance fields that can be used to define future and ongoing training and aircraft performance requirements and specifications, such as ADS-33 [8].

Technical Objectives

The goal of the effort is to develop a fundamental understanding of the relationship between the length and time scales typically present in disturbance fields experienced by Naval aviators (i.e. ship airwakes, wing wakes etc.) and rotorcraft FD and FQ when the fully-interacting fluid dynamics of the airwake and rotor wake and flight mechanics are accounted for. With this information in hand, the engineering community would be better able to understand the relationship between aircraft type, ride quality, FD and FQ during flight conditions where disturbance fields are encountered. The community would be able to more accurately define trainer requirements, minimum experimental campaign requirements, minimum CFD modeling requirements and consequently establish a benchmark to evaluate CFD predictive capability. Furthermore, the conclusions of this work would also directly impact the development of requirements for new aircraft given the direct correlation between FD and FQ. The proposed effort would undertake the research required to develop such an understanding, with disseminating the observations and conclusions of the work to the Navy and the broader FD, FQ and handling qualities communities - a key objective from the outset. The effort will be structured using a build-up approach that first focuses on defining relevant disturbance fields followed by predicting and understanding the fundamental aeromechanics response (i.e. aerodynamic forces and moments and rotor dynamics). The effort would culminate in predicting the flight dynamics and handling qualities for realistic, but generic, helicopter and tiltrotor configurations that include representations of flight controls, propulsion system and cross-

coupling characteristics. The key objectives for the effort roughly form the main tasks and are as follows:

1. Define the spatial and temporal fluid dynamic scales present in relevant disturbance fields and develop numerical representations for testing (Year 1).
2. 6-DOF generic model assembly and shakedown testing to ensure correct operation and functionality.(Year 1)
3. Define aeromechanics performance and HQ metrics along with a detailed simulation test matrix that includes systematic and consistent model fidelity build-up (Year 1-2).
4. Undertake simulation of a generic helicopter interacting with frozen and distorting disturbance fields to establish fundamental response characteristics (Year 2).
5. Undertake simulation of a generic tiltrotor interacting with frozen and distorting disturbance fields to establish fundamental response characteristics (Year 2).
6. Develop a realistic full helicopter model and undertake simulations of interactions with frozen and distorting disturbance fields to establish flight dynamics and handling qualities response (Year 3).
7. Develop a realistic full tiltrotor model and undertake simulations of interactions with frozen and distorting disturbance fields to establish flight dynamics and handling qualities response (Year 3).
8. Documentation and dissemination of observations and conclusions to the Navy and the wider FD/HQ community (Years 1-3).

Summary of Work Conducted During Reporting Period

During this progress period, work has continued on the development and testing of the method for formulating canonical airwake presented in the previous progress report. In addition, CDI has obtained permission to access and use the Navy's CASTLE simulation environment, and a copy of the example helicopter model and the latest version of CASTLE and associated software components were provided by NAVAIR to CDI in August. CDI has a prior version of CASTLE etc installed and running, and we are currently working with NAVAIR engineers to determine whether multiple versions of CASTLE can be installed at one time and on verifying that the software has been installed correctly and is working as expected.

Simplified Wake Representation

Summary of Work Conducted During Reporting Period

During this progress period, work has continued on the development and testing of the method for formulating canonical airwake presented in the previous progress report. Analytical model fitting was performed on various 2D planes for time-averaged longitudinal velocities obtained from CFD simulations of a headwind over a cube, which is a representative canonical shape. Model input parameters, and their spatial variation in the various 2D planes considered provide quantitative insights into the primary coherent structures present in the flow, as well as their spatial evolution. Three-dimensional (3D) reconstruction of the time-averaged longitudinal velocity field was also performed, demonstrating the adequacy of the analytical models in capturing general flow behavior. Initial results using the analytical models were presented in previous quarterly demonstration reports, where we determined the fitting parameters by performing manual tuning to best match the CFD data. During the current reporting period, the

manual tuning scripts were overhauled and replaced by modular and automated scripts that automatically determine model parameters using an error minimization procedure. Work is currently underway for time-averaged vertical velocity profile fitting, and initial results will be presented in this report. In addition to time-averaged spatial characterization of flow features, we also examined the spatiotemporal characterization of flow *dynamics* using a multi-resolution proper orthogonal decomposition approach during the present reporting period. Results from this characterization supplement those from the time-averaged analyses and provide quantitative assessments of the turbulent kinetic energy associated with each coherent feature *and* their corresponding frequencies (time scales). Initial results from this dynamic characterization will be presented. The time-averaged and dynamic characterization of flow features collectively represent parametrizable metrics that can be employed to generate representative airwake in the vicinity of differing ship geometries and/or varying freestream velocities, without having to resort to explicit CFD simulations. Note that the work presented here builds upon early work performed under a concurrent effort for NASA (Contract No. 80NSSC21C0026) that aims to develop a ride quality assessment tool for urban air mobility (UAM) aircraft.

A description of the CFD simulations is provided next for reference. The remainder of the report is then divided into two main parts: time-averaged characterization and dynamic characterization.

CFD Simulation

CFD simulations were performed using the CDI CGE/VorTran-M flow solver. CDI's adaptive cut-cell octree Cartesian Grid solver (CGE) is a Cartesian grid solver that solves the compressible URANS equations using either a Spalart-Allmaras (SA) or a shear stress transport (SST) turbulence model and resolves boundary layers and other highly anisotropic flow features in an efficient manner using wall functions. The VorTran-M (VTM) model simulates the evolution of initial vorticity distributions in unbounded domains. The CGE/VorTran-M coupled arrangement consists of implementing the CGE solution on the grid as an "inner" solver that extends sufficiently far to contain regions with significant compressibility or flow turbulence and VTM as an "outer" solver that is applied in the essentially incompressible flow region and efficiently transports the vorticity with minimal dissipation. Such an arrangement allows for computational savings in mesh resolution when compared to a solely CGE-based simulation. This coupled setup has been previously used for both ship and urban airwake modeling.

Development of canonical airwake models has centered on flow simulation over a simple cube. Primary flow features associated with a headwind flow over a cube are illustrated in Figure 2 and include

- A horseshoe vortex that forms upstream of the obstacle where the flow stagnates and wraps around the cube (feature "A" on the figure);
- On the top and side surfaces, local separation and reattachment regions ("B" and "C" on the figure);
- In the lee of the obstacle, an arch vortex (feature "D" on the figure) that forms due to the separation of the shear layers from the top and side surfaces. The streamlines aft of the obstacle indicate a recirculation region, where the direction of the flow reverses.

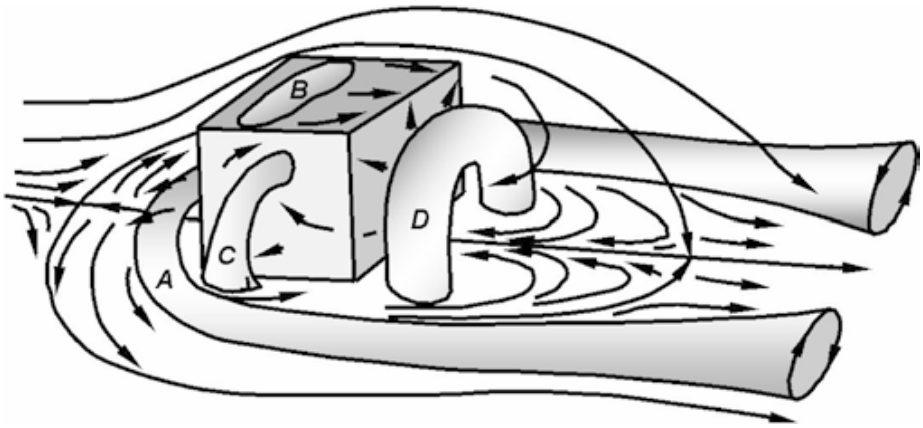

Figure 2: Schematic of principal flow features around surface-mounted obstacle [9].

To generate source data for canonical model development, CFD simulations were performed for a 30 m/s headwind over a 10 m cube. Although this speed is larger than would be typically encountered in practice, it is necessary to use a larger freestream velocity to maintain good numerical conditioning of the compressible flow solver. An alternative approach would have been to take advantage of the preconditioners implemented in CGE for low-speed flows. However, we deemed using the higher velocity appropriate given that the flow field is dominated by separation from the sharp edges of the cube, which has a weak dependence on viscosity. This further allowed us to perform simulations for inviscid flow only. Neglecting viscosity effects allows for scaling of time-accurate flow predictions using freestream velocity. This scaling has also been confirmed in viscous flow simulations for geometric configurations representative of the operating environments of rotorcraft. Note that no explicit atmospheric boundary layer (ABL) model was included in the simulation. Simulations were performed using a fixed time step of 0.005 seconds. A steady CGE only simulation was first carried out to obtain a starting estimate for the transient coupled CGE/VorTran-M solution. This sequence enables an expedient solution that does not require the code to resolve and propagate the starting vortices far downstream, as would otherwise be expected from an impulsive start. The transient simulation was then carried out for a duration of 25 seconds, where there first three seconds were used for transition from steady to transient simulation and the subsequent 22 seconds worth of data were recorded for post-processing in 0.1s increments. Vortex shedding frequency is characterized by the Strouhal number, which is defined as

$$St = \frac{fb}{U} \tag{1}$$

where f is the vortex shedding frequency and b is the characteristic length. Results from literature indicate dominant periodicity for flow aft of a cube at a distance of 6H [10] to have a characteristic frequency of $St = 0.104$ [10, 11], where H is the cube height. Using 10 m cube length as characteristic length and the freestream velocity of 30 m/s as characteristic velocity, this Strouhal number corresponds to a vortex shedding frequency $f = 0.3$ Hz, which, in turn, corresponds to a period of 3.2 seconds. The trimmed 22 second simulation duration thus allows for approximately 7 cycles of vortex shedding to be captured. CFD results were compared to results from literature in previous progress reports.

Six primary flow features were identified from the simulations, illustrated in Figure 3. Note that the von Karman vortex street shown in Figure 3(e) is only observed during *time-accurate*

solutions. Contours of *time-averaged* longitudinal velocity instead display a symmetrical distribution aft of the obstacle as evident in Figure 4(b). Two dimensional analytical models were fit onto these features to capture the associated longitudinal velocity profiles. Two-dimensional models were chosen as starting point for simplicity and because they provide a basis for a fundamental, "ground-up" approach to airwake reconstruction. The planes shown in Figure 4 contain these features and were used as reference planes for model fitting. The right-handed coordinate system shown in Figure 4 has its origin at the center of the bottom face of the cube. Freestream is in the negative z direction. All position coordinates in this report are defined relative to this coordinate system unless stated otherwise.

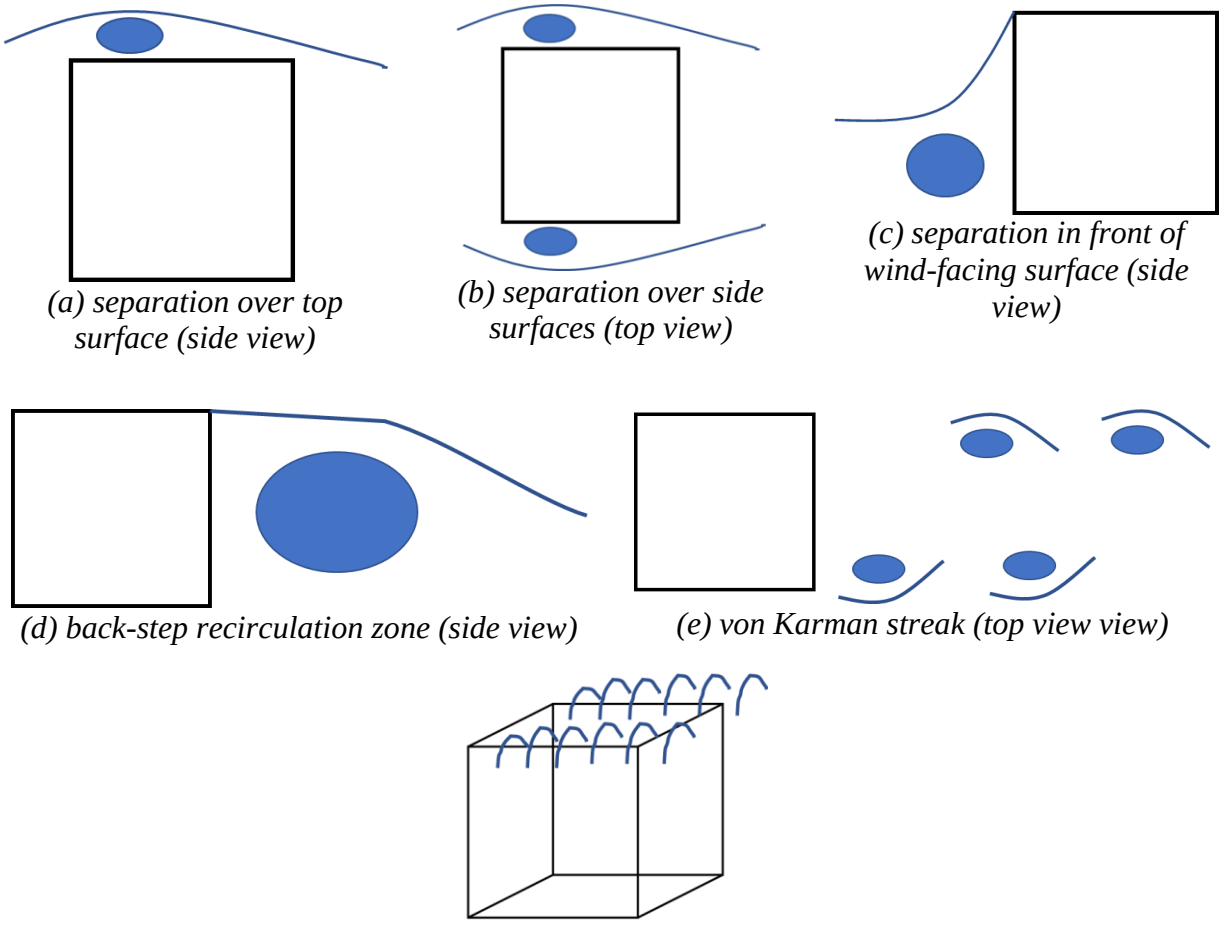

(a) separation over top surface (side view)

(b) separation over side surfaces (top view)

(c) separation in front of wind-facing surface (side view)

(d) back-step recirculation zone (side view)

(e) von Karman streak (top view view)

(f) edge vortices on top surface that develop due to pressure gradients between side and top surfaces (perspective view)

Figure 3: Primary flow features identified from CGE/VorTran-M simulation of 30 m/s headwind over 10m cube (Freestream direction from left to right)

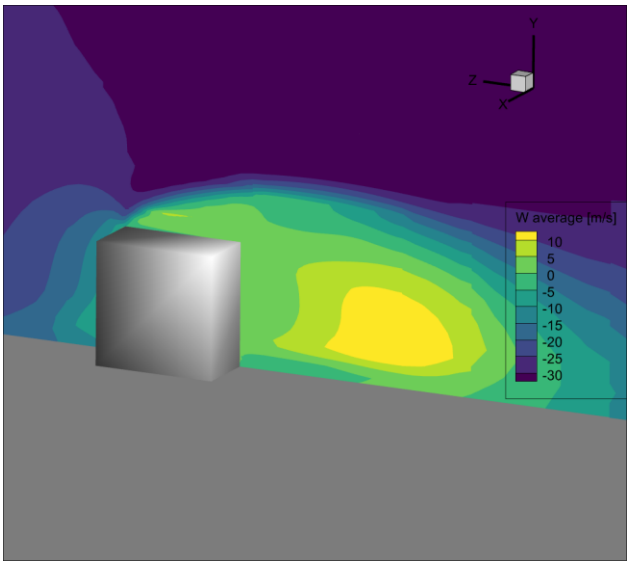

(a) x=0m midplane showing top surface separation and back step recirculation

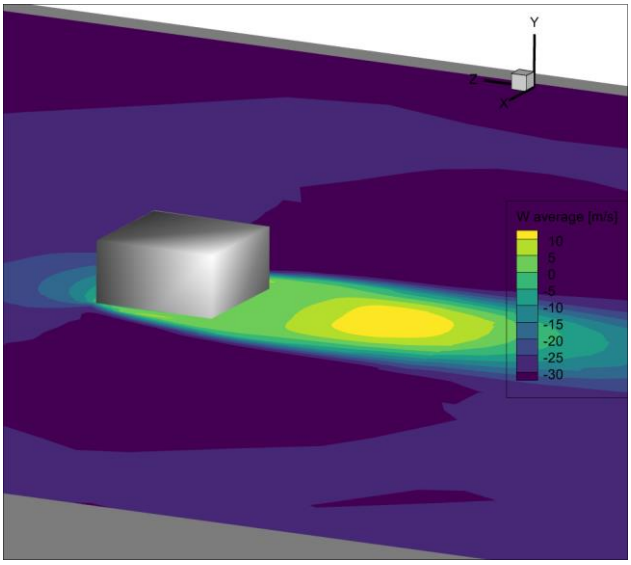

(b) y=5m midplane showing side surface separation and symmetrical aft recirculation

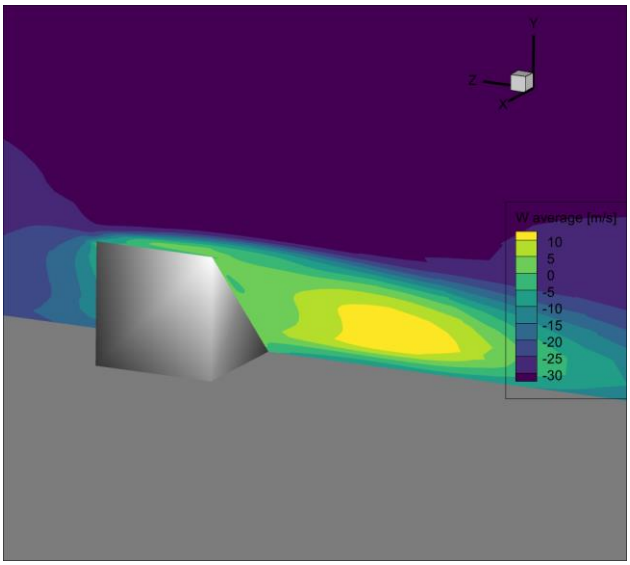

(c) diagonal plane that capture corner edge separation and aft recirculation

Figure 4: Contour of time-averaged longitudinal velocity for a 30m/s headwind simulation over a 10m cube using CGE/VorTran-M along planes containing primary flow features.

Time-Averaged Characterization

Analytical model fitting was performed for longitudinal velocity along the planes shown in Figure 4. The models employed are described in this section for reference, along with representative 2D and 3D airwake reconstruction results. This is followed by a description of the automated parameter extraction procedure and initial results for vertical velocity profile fitting and parameter variation.

Analytical vortex models

The vortex model proposed by Banks and Meroney [9, 12] was used as basis for the analytical model. A depiction of the vortex model proposed by Banks and Meroney is shown in Figure 5 [9]. A vortex of radius h with center at point O is placed above the surface such that it touches the surface at point S. To allow for a smooth transition from constant vorticity within the vortex to regions of zero vorticity where potential flow theory applies, a transition region is introduced, with point M on Figure 5 indicating the start of the potential flow region. Point C represents the location of maximum velocity in the transition region and is typically set to the midpoint location in the transition region. The vortex is envisioned to be driven like a wheel, spinning due to freestream velocity acting at point M [9]. Banks and Meroney provide piece-wise continuous expressions for velocity across five distinct regions of the domain, shown in Figure 6. The nondimensional coordinate $a = \zeta/h$ will be used when referencing distances relative to the vortex center. The core is assumed to have a diameter of $0.2h$ and represents a region dominated by viscosity, where flow follows a solid body rotation motion. In the region between the core and transition ($0.2 < a < 1$), the velocity profile is based on a power curve fit to the velocity profile obtained from a Navier-Stokes based simulation for a 65° swept delta-wing at a 10° angle of attack at 70% chord and Mach number $Ma = 0.85$. This relation is used because of the similarity between conical vortices on the roof of a building and delta-wing vortices observed on delta-wing aircraft. Between the core and roof surface (-1 < a < 0.2), pressure changes occur due to centrifugal accelerations of the vortex, such that the resulting governing equation is (see [9]):

$$\frac{dP}{dn} = \frac{\rho U^2}{R_c} \tag{2}$$

where P is the pressure, n is the unit normal to the curvature, ρ is the fluid density, U is the fluid speed in the direction of the vortex, and R_c is the radius of curvature. In the potential flow region, flow merges with freestream and both Bernoulli's equation and Eq. (2) are obeyed. The equations representing the velocity profile from this model are summarized in Table 1. There are three primary inputs to the model:

1. vortex radius (h),
2. location of point M (R_M), and
3. velocity at point M (U_M).

Table 1: Velocity profile equations for Banks and Meroney vortex model [12]; $\boldsymbol{a_1 = 0.2}$ is used to delimit vortex core size, $\boldsymbol{a_2 = 1}$ is used to delimit vortex size, $\boldsymbol{a_3}$ is used to demark start of potential flow region, $\boldsymbol{a_{max}}$ is used to denoted the point in the transition region where maximum velocity is obtained, $\boldsymbol{U_{max}}$ is taken to be the velocity at point M, $\boldsymbol{U_{a_1} = U_{vortex}(a_1)}$, $\boldsymbol{U_{a_2} = U_{transition}(a_2)}$, $\boldsymbol{U_{a_3} = U_{tranistion}(a_3)}$ and $\boldsymbol{n' = n/h}$.

R_c/h	Range	Description	Velocity Equation
$-\infty$	$a = -1$	Roof surface	$U = 0$
$a/(1+a)$	$-a_2 < a < -a_1$	Between roof and vortex core	$U(a) = -U_{vortex}(a) = -U_{a_2} \cdot \sqrt{a/-a_2}$
a	$\lvert a \rvert < a_1$	Viscous vortex core	$U(a) = U_{core}(a) = U_{a_1} \cdot a/a_1$
$a + a^3/2$	$a_1 < a < a_2$	Vortex, above core	$U(a) = U_{vortex}(a) = U_{a_2} \cdot \sqrt{a/a_2}$
$a + a^3/2$	$a_2 < a < a_3$	Transition region	$U(a) = U_{transition}(a) = \frac{U_{max} \cdot 2 \cdot (a/a_{max})}{1 + (a/a_{max})^2}$
$a + a^3/2$	$a_3 < a$	Potential flow region	$U(a) = U_{potflow}(a) = U_{a_3}\sqrt{e^{\int_{a_3}^{a} \frac{-2}{(R_c/h)} dn'}}$

Sample results for the longitudinal velocity at two locations on the top of the surface along the midplane shown in Figure 4(a) are shown in Figure 7, where the model adequately captures the velocity profiles predicted by CGE/VorTran-M.

A modified version of the model was introduced to capture longitudinal velocity profile associated with the separation aft of the obstacle (seen in the contours in Figure 4). The equations in Table 1 were still applied but in this case, the vortex was shifted upwards such that a transition region existed below the vortex center as well, as depicted in Figure 8. With this shift, the vortex model can be thought of as wheel being spun at two points: point M_{upper} at a velocity $U_{M_{upper}}$ and point M_{lower} at a velocity $U_{M_{lower}}$. The vortex core size, which was previously set to $0.2h$, was allowed to vary. Additionally, closer to the ground, the longitudinal velocity was set to a constant ground velocity (U_0), which, in most cases, was set to zero. Since we are using results from an inviscid simulation as truth model, velocity at the ground is not necessarily always zero. Inputs to the modified model consisted of

1. location of vortex center (r_c).
2. vortex radius (h),
3. vortex core radius fraction (c)
4. location of point (M_{upper}),
5. location of point (M_{lower}),
6. velocity at point M_{upper} ($U_{M_{upper}}$),
7. velocity at point M_{lower} ($U_{M_{lower}}$),
8. location of point close to ground (y_g) below which the constant velocity was assumed, and
9. velocity near ground (U_0).

Sample results are given in Figure 9 for z=-18m along the mid plane shown in Figure 4(a).

The two versions of the Banks and Meroney model allowed for 1D predictions of longitudinal velocities at specified span (z) locations along the midplane (Figure 4a). The inputs to the models provide basis for eventual parametrization and scaling. For 2D predictions over the top surface, polynomial functions were derived for the model inputs as a function of span location z using the parameters obtained via manual fitting at multiple span locations. This extension to 2D effectively assumes that an infinite number of overlapping vortices of differing sizes exist in that plane. Aft of the obstacle, a piece-wise approach was taken where the vortex was assumed to have an ellipse shape in the vicinity of the obstacle and the infinite vortex model was employed further downstream. Details on these implementations and application to velocity profiles along the transverse plane (Figure 4b) were provided in the previous progress reports. During the present reporting period, a similar polynomial-based model fitting approach to that described in the previous paragraph was implemented to capture the longitudinal velocity profile over and aft of the obstacle along the diagonal plane shown in Figure 4(c).

Results from using this piece-wise modeling approach are shown in Figure 10 and Figure 11 for the region aft of the cube along the midplane shown in (Figure 4a). These plots allow for quantitative characterization of length scales associated with different flow features. For instance, in Figure 10, we note that the velocity in the lower transition region is close to 0 m/s at z=-6m (immediately aft of the obstacle), becomes progressively more positive up to a peak of ~14m/s at z=-18m and starts reducing in magnitude beyond that. This trend is associated with the recirculation region seen in Figure 4a. In Figure 11, we note that the velocities in the lower transition and near the ground are all negative, indicating that the effect of the recirculation region becomes progressively less prevalent further downstream.

It is important to emphasize here that the even though the model proposed by Banks and Meroney is a vortex model, we refer to the versions adopted here as "analytical" models as they are primarily used as mathematical constructs that were found to represent CFD source data. Although model input parameters provide insights into physics of flow features, proper physical characterization of these features as vortex phenomena such as point vortices, vortex lines or sheets was not a focus in this work thus far and will be re-examined as necessary.

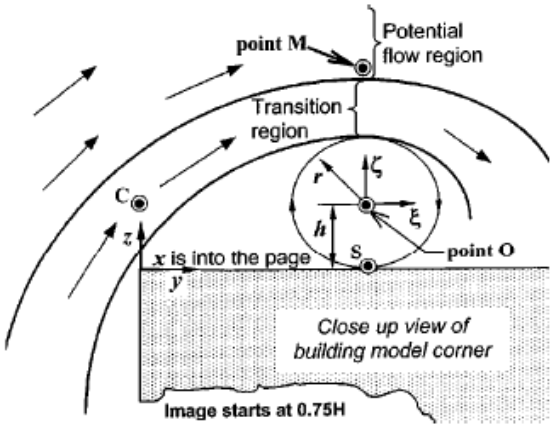

Figure 5: Illustration of the vortex model proposed by Banks and Meroney [9].

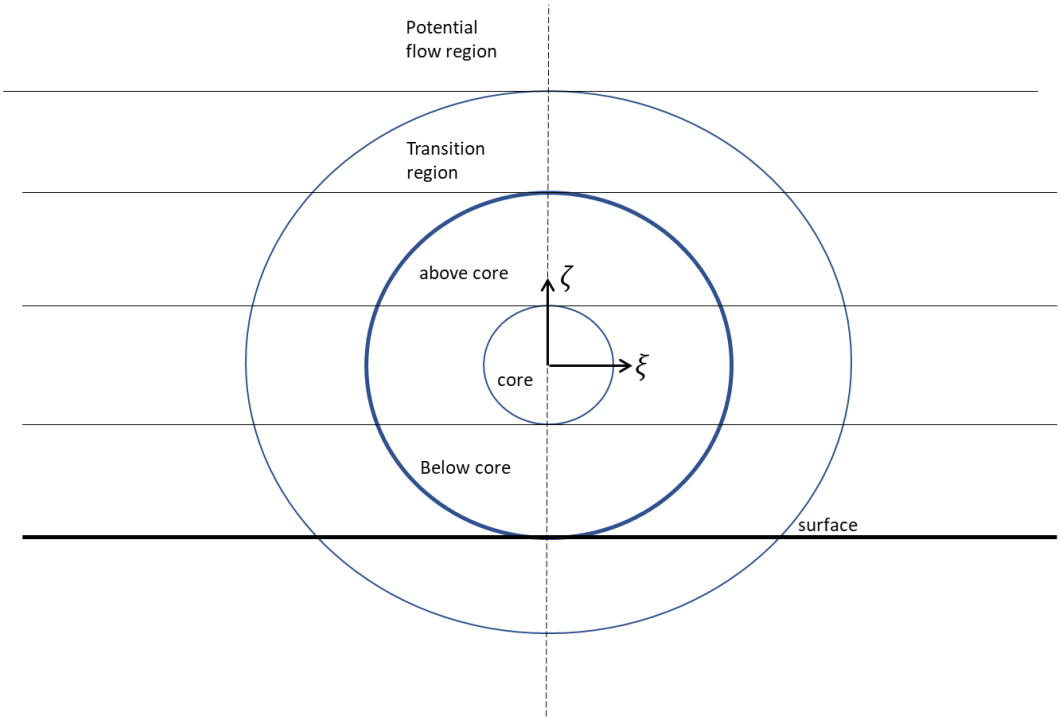

Figure 6: Illustration of the vortex model proposed by Banks and Meroney highlighting the five regions considered.

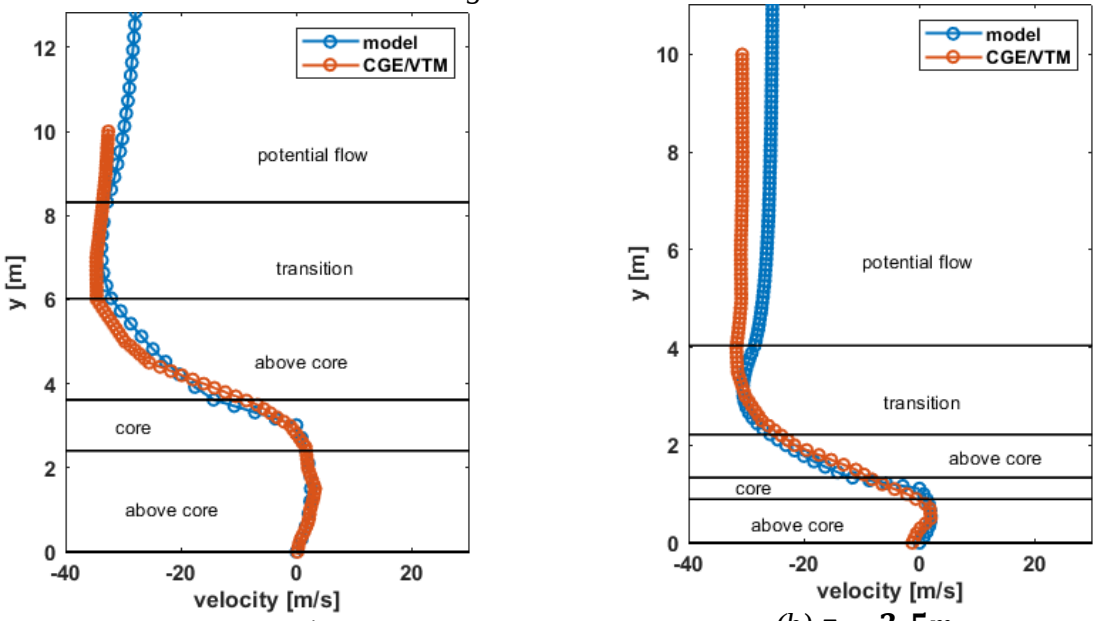

(a) $\boldsymbol{z = -3.5m}$ *(b)* $\boldsymbol{z = 3.5m}$

Figure 7: Longitudinal velocity profile at two span locations over top surface of cube; height plotted relative to top surface.

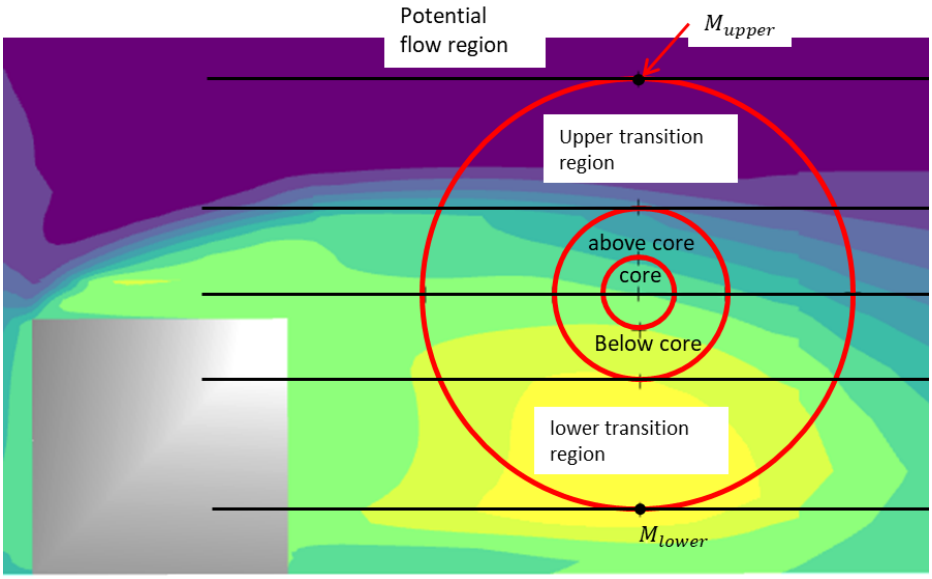

Figure 8: Illustration of modified Banks and Meroney vortex model shifted upwards.

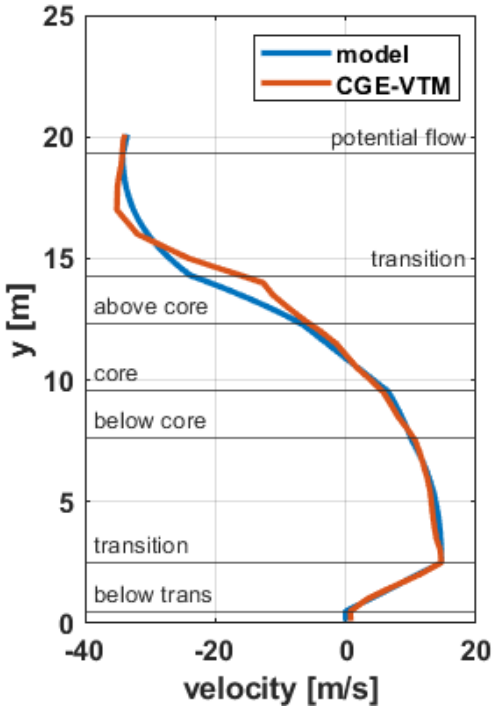

Figure 9: Longitudinal velocity profile along a vertical line through z=-18m in the lee of the cube.

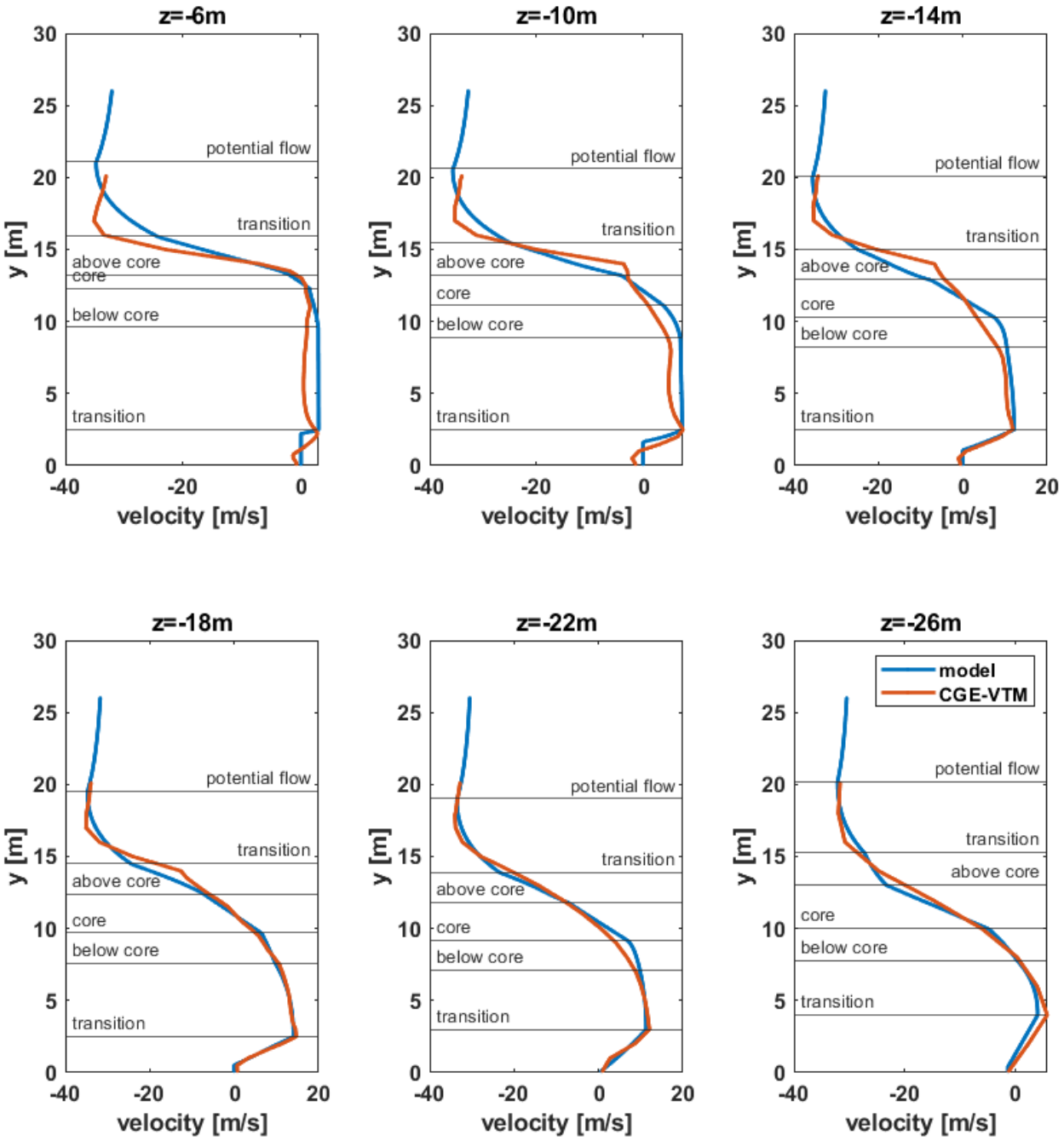

Figure 10: Longitudinal velocity profile at various span locations aft of the obstacle along the $x = 0$ m plane using the slanted ellipse-based vortex model for $-6\ m \geq z > -26\ m$ and the infinite vortex model for $z = -26\ m$; CGE/VorTran-M data queried in 0.1 m height increments at every span location.

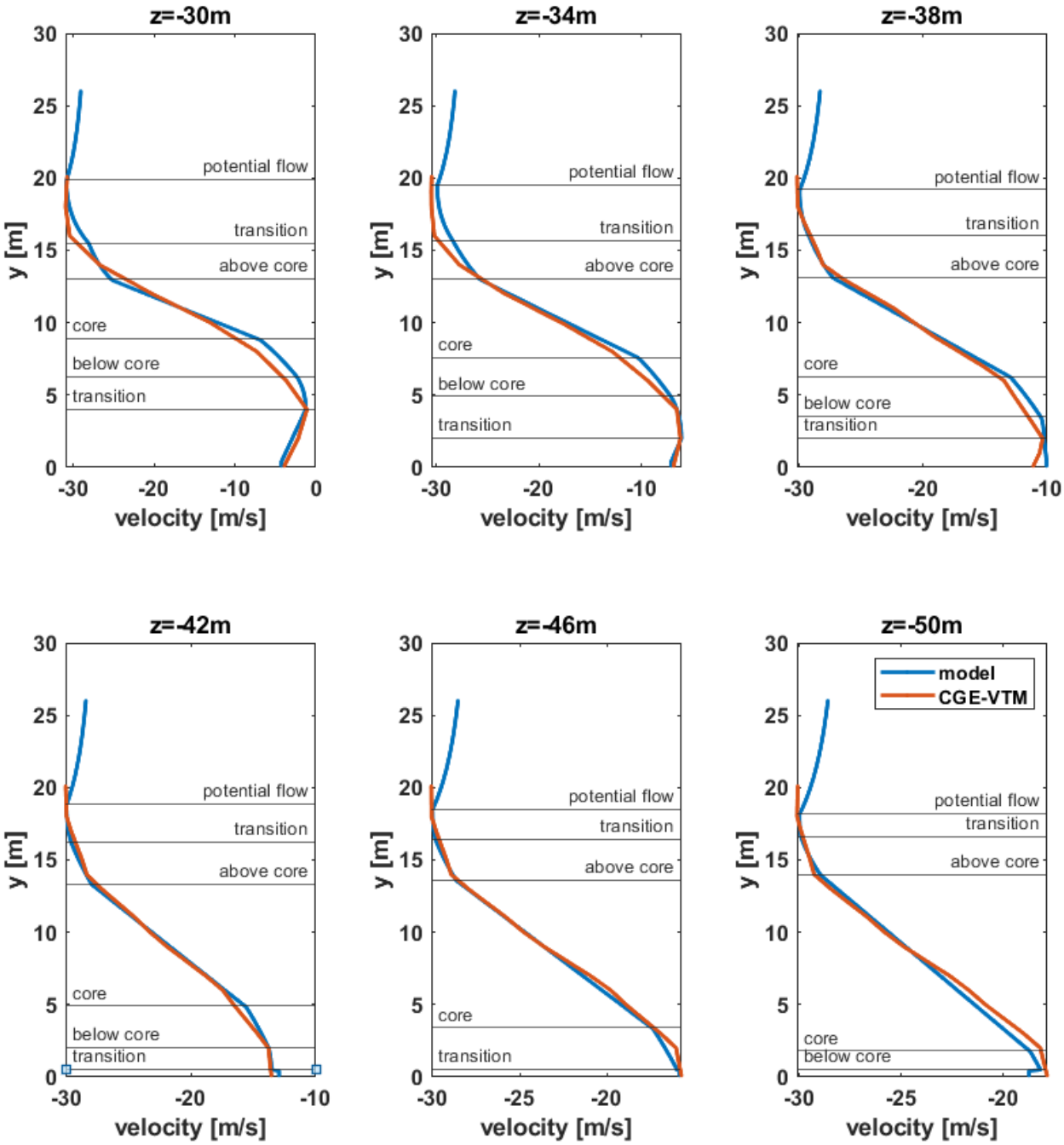

Figure 11: Longitudinal velocity profile at various span locations in the $-30\ m \geq z \geq -50\ m$ range aft of the obstacle along the $x = 0\ m$ plane using the infinite vortex model; CGE/VorTran-M data queried in 0.1 m height increments at every span location.

3D Longitudinal Velocity Field Reconstruction

The analytical models adequately captured time-averaged longitudinal velocity profiles across the three planes shown in Figure 4. We performed 3D reconstruction of the longitudinal velocity profile to further test the viability of the models. We generated a database of position coordinates and corresponding velocities along the three planes and used MATLAB's

`scatteredInterpolant`[1] capability to "blend" the velocities for 3D reconstruction. Provided a 2D or 3D scattered dataset, this MATLAB function returns a function handle that outputs interpolated values for user specified position coordinates. This capability supports several interpolation and extrapolation methods. In this work, we employ the `linear` method for interpolation and extrapolation.

To evaluate the parametric model velocity field reconstruction, predictions were made along the transverse plane shown in Figure 12. Corresponding results are shown in Figure 13 and show good agreement between the model predictions and CGE/VorTran-M data. The discontinuities noted in the analytical contours represent the planes along which the 2D model fitting was performed. Note that an additional horizontal plane at y=3m was employed to obtain the results shown in Figure 13. These results further confirm the viability of the analytical models.

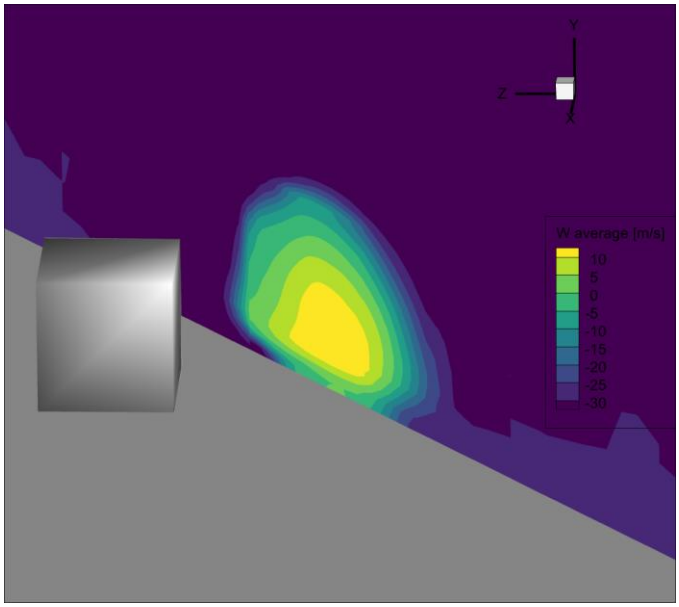

Figure 12: Transverse plane considered in parametric model evaluation.

[1] https://www.mathworks.com/help/matlab/ref/scatteredinterpolant.html

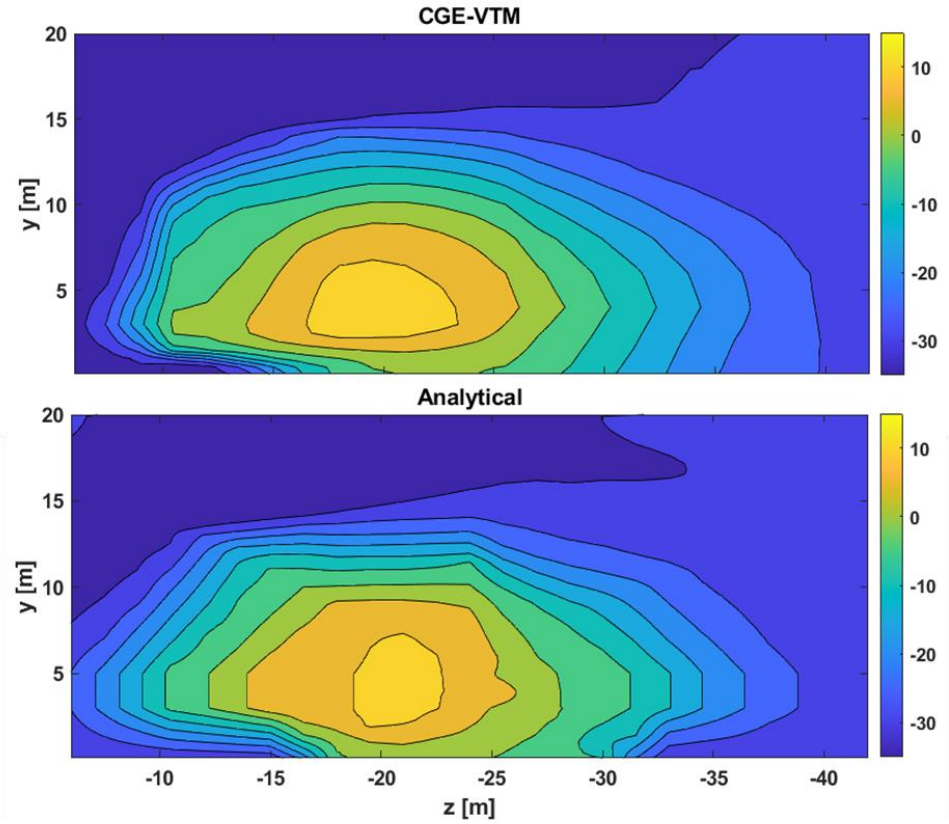

Figure 13: Mean longitudinal velocity contours along transverse plane; truth (top) and parametric model (bottom).

Automation of Parameter Extraction

The 3D velocity reconstruction results presented in the previous section gave confidence in the canonical airwake modeling approach. Work was performed to overhaul the previous model implementation scripts, which were based on manual tuning, and replace them with modular parameter extraction scripts that automatically determine model fitting parameters via an optimization procedure using MATLAB's `fmincon` function. The optimization problem formulation consisted of varying model input parameters to minimize the error between truth and 1D model prediction data subject to lower and upper bounds on parameter values. To expand the predictions to 2D planes (for instance, along the top surface region of the midplane shown in Figure 4a), an outer level script was written to automatically perform optimization-based parameter extraction at multiple span locations (along the z axis) to obtain polynomial functions for the model input parameter variation. To further expand the predictions to 3D, an additional script that performed automatic model fitting along a transverse (x axis) plane was implemented. This script was used to determine polynomial functions for *changes* in model parameters. As such, longitudinal velocities along the vertical line through any position coordinate on the top surface obstacle could be determined using model input parameters obtained as follows:

$$\mathrm{X} = \mathrm{X_L} + \Delta\mathrm{X_T}, \tag{3}$$

where X is a generic variable to represent a model input parameter, X_L represents the value of the parameter obtained using the spanwise z coordinate polynomial functions, and $\Delta\mathrm{X_T}$ represents

the change in X_L as function of the transverse x coordinate. The scripts are modular such that model input parameters for 1D, 2D, and 3D spatial domains can be readily setup and obtained.

Vertical Velocity Fitting

Work is currently underway to perform model fitting of mean vertical velocity profiles, which is particularly important for the ship-helicopter dynamic interface given that this velocity component directly influences rotor inflow, which, in turn, affects rotor loads and consequently, aircraft flight dynamics and handling qualities. Initial tests were performed using the modified Banks and Meroney model described above. However, the model was not globally applicable to all locations in the domain. We thus devised a custom piece-wise analytical model for the fitting consisting of first and second order polynomials. This is depicted in Figure 14, which shows a typical vertical velocity profile and the four regions where polynomial fitting is performed. A linear fit is employed in regions #1 and #3 and a second order fit in regions #2 and #4. Model input parameters consist of:

1. velocity near ground (v_0);
2. location where region #1 ends and region #2 starts (r_1);
3. velocity at r_1 (v_1);
4. location where region #2 ends and region #3 starts (r_2);
5. velocity at r_2 (v_2);
6. velocity in the middle of region #2 (v_{2m});
7. location where region #3 ends and region #4 starts (r_3);
8. velocity at r_3 (v_3);
9. location where region #4 ends (r_4);
10. velocity at r_4 (v_4); and
11. velocity in the middle of region #4 (v_{4m}).

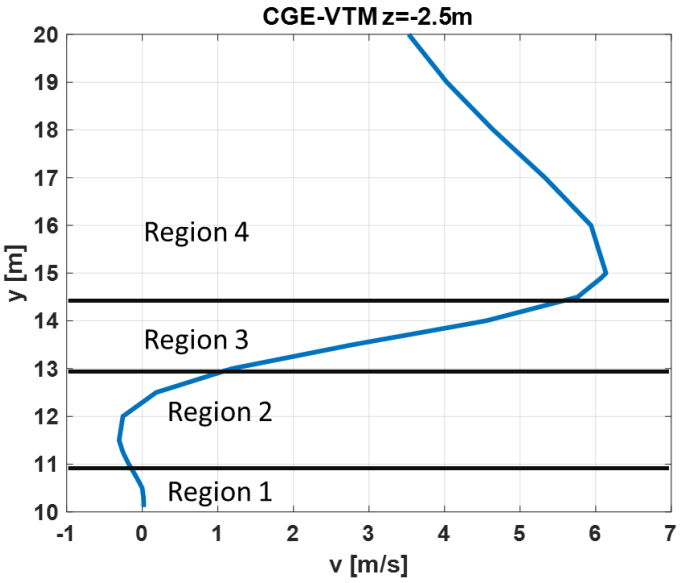

Figure 14: Typical vertical velocity profile from CGE/VorTran-M highlighting the four regions considered in the fitting model.

Model fitting results for the vertical velocity profile over the top surface along the midplane shown in Figure 4(a) are shown in Figure 15. We used the automated scripts to determine the optimal parameters. Note that velocities near the ground are not necessarily zero. This is because CGE/VorTran-M enforces the no-penetration boundary condition at walls by setting the convective flux, not velocity, through the cell face corresponding to the wall to zero. The model shows good agreement with CGE/ VorTran-M results. Regions #3 and #4 are the primary ones present closer to the leading edge at z=5m and z=2.5m. As we proceed further downstream, region #2 emerges indicating the presence of recirculation. This is evident from the slight negative vertical velocities noted at z=-2.5m in the $y \in (0,2]$m range and further confirmed from the Tecplot contour plot of time-averaged vertical velocity and shown in Figure 16.

Similar results were obtained for the vertical velocity profile on either side of the obstacle (along the midplane shown in Figure 4(b)) and along the diagonal edge of the obstacle (along the plane shown in Figure 4(c)). Work is underway to capture the vertical velocity profiles aft of the obstacle along the same planes.

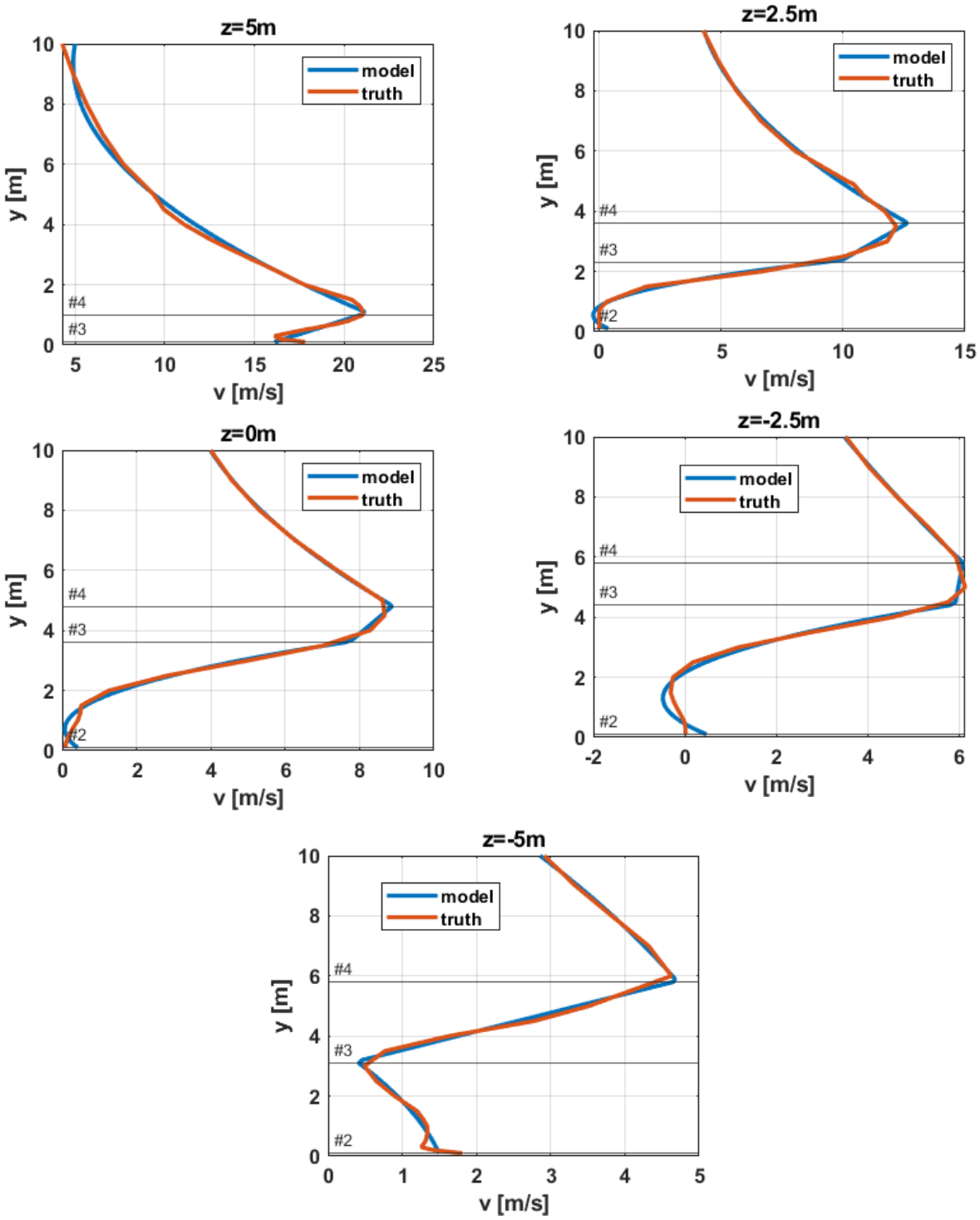

Figure 15: Time-averaged vertical velocity over top surface along x=0m plane.

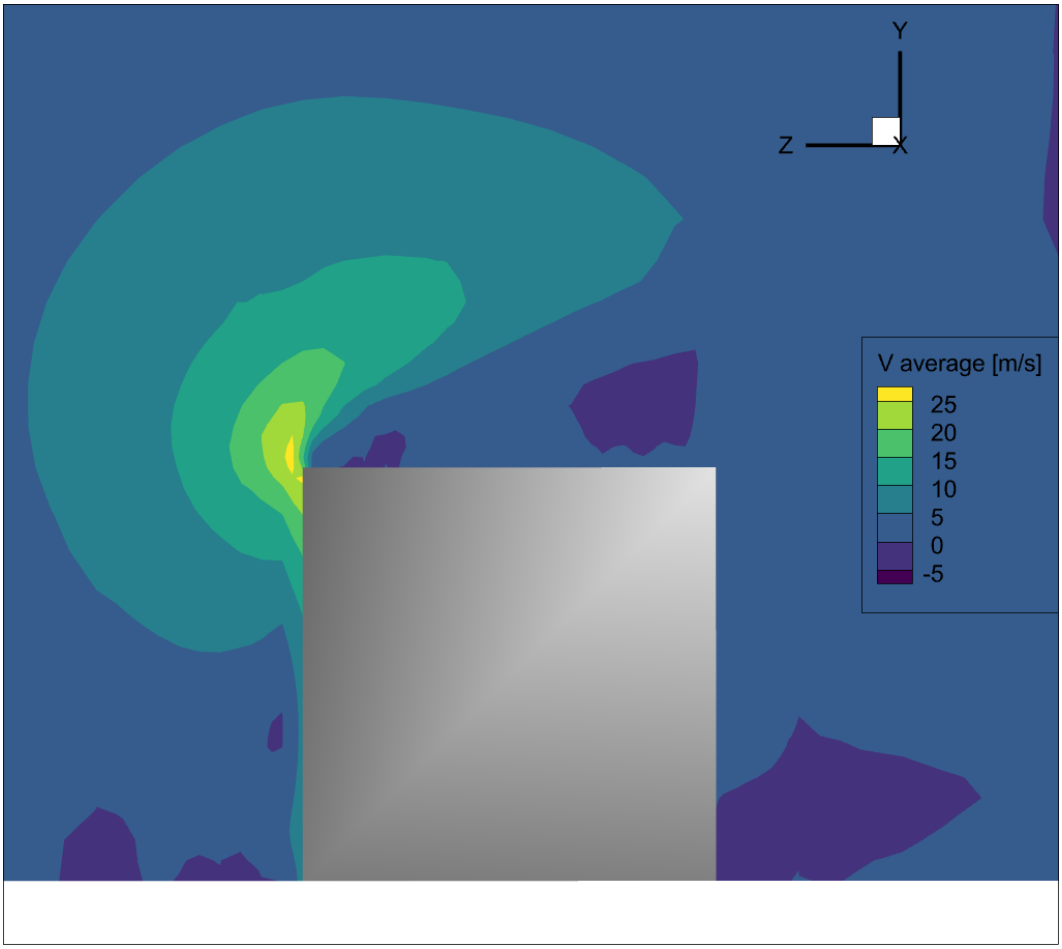

Figure 16: Time-averaged vertical velocity contour along x=0m plane from Tecplot.

Dynamic Characterization

A spatiotemporal characterization of the flow features shown in Figure 3 and Figure 4 is critical for a better understanding of the ship-helicopter dynamic interface. Although this fact is generally accepted, work in literature has typically focused on the identification of coherent structures with limited characterization of the time dynamics associated with them. Spatiotemporal characterization of fluid dynamics is typically performed using modal decomposition methods that attempt to represent unsteady flows with random fluctuations as superpositions of deterministic basis vectors or "modes" that can provide better insights into flow behavior [13]. Two popular methods are the proper orthogonal decomposition (POD) [13-16] and dynamic modal decomposition method (DMD) [17-20].

The POD method follows the classical separation of variables approach to solving partial differential equations (PDEs) and represents quantities of interest (e.g., velocity) as a superposition of spatial basis vectors and corresponding temporal coefficients. Emphasis is typically placed on determining the orthonormal spatial basis functions that are computed using the spatial covariance matrix of quantities of interest (e.g., velocity, pressure) [13]. The temporal coefficients are determined from the spatial basis vectors and provided quantity data. The

covariance matrix indicates how a change in a quantity of interest at any given spatial location is associated with changes in the rest of the domain. That is, it gives a measure of data correlation, which, also gives a measure of turbulent kinetic energy (TKE) when the quantity of interest is velocity [13]. The TKE is a metric used to quantify flow turbulence and is defined as [21]

$$TKE = \frac{1}{2}\left(\overline{u'^2} + \overline{v'^2} + \overline{w'^2}\right), \tag{4}$$

where, $\overline{u'}, \overline{v'}, \overline{w'}$ represent average fluctuating longitudinal, lateral, and vertical velocity components,

$$\overline{u'} = \frac{1}{T}\int_0^T (u(t) - \bar{u})\, dt, \tag{5}$$

and where $u(t)$ is the instantaneous velocity and $\bar{u}$ is the average velocity at the location. The $\overline{v'}$, and $\overline{w'}$ terms have similar definitions. The spatial modes obtained using POD are orthonormal and each have different TKE levels associated with them. The most energetic ones can be further examined to identify primary coherent structures responsible. The POD method is considered an energy decomposition method [15]. A downside of the method, however, is that each mode can be associated with a wide range of time scales (frequencies), making a proper spatiotemporal characterization of flow features a nontrivial task.

The DMD method on the other hand, is a frequency decomposition method where each resulting mode is associated with one unique frequency, thus providing information on both the length- and time scales of coherent structures [15, 17, 19]. In this method, nonlinear systems are mapped onto a linear space (generally with infinite-dimension) using a linear operator. The formulation is such that eigenvalue decomposition of the linear operator allows for the identification of coherent structures in the flow using the DMD modes, and their growth/decay rates and frequencies using the eigenvalues. Note that the DMD modes are different from the eigenvectors obtained from eigenvalue decomposition [17, 19]. The DMD modes are not ranked by energy levels and are not orthonormal. Since both spatial *and* temporal aspects are considered in the DMD characterization, various criteria have been proposed to identify the dominant DMD modes, each with varying performance for given flow configurations [17]. This method is generally preferred for flow reconstruction of periodic system since it places emphasis on spectral purity of the decomposition (distinct frequencies for each mode). For unsteady, nonlinear systems, frequency modulations, phase jitter and other localized frequency events are not readily captured. Moreover, the large number of modes required to capture major flow dynamics in the time domain often leads to redundancy in the structure of the spatial domain [15].

Given the limitations of POD and DMD methods, several hybrid methods have been developed to characterize flow dynamics in terms of energy content and spectral purity. In this work, we employ a multi-resolution POD method proposed based on the recent work by Zhu et al. [16], where frequency ranges or "bins" that contain the most energetic features are first identified, before performing POD to identify the associated coherent structures. Resolving the energetic features into frequency bins allows for a more intricate spatiotemporal characterization of flow dynamics, when compared to the traditional POD method, as the frequency ranges are typically narrow and more specific to coherent structures.

The multi-resolution POD approach is described next, followed by initial results obtained. The quantities of interest in this work will be the longitudinal and vertical velocity components.

Multi-Resolution Proper Orthogonal Decomposition

Several coherent structures spanning a range of length and time scales exist in typical ship airwake. For the ship-helicopter DI, the most energetic coherent features are of interest since these influence aircraft flight dynamics and handling qualities. The multi-resolution POD method isolates these coherent features by identifying and analyzing airwake data only within frequency ranges where these energetic features exist [16]. There are three primary steps involved: (a) identify the most energetic features and the N_{bin} frequency bins in which they exist, (b) filter the original data using bandpass filters to generate N_{bin} datasets corresponding to the ranges of each frequency bin, and (c) perform POD of the individual filtered datasets to identify the primary coherent features within each frequency range. This approach allows for a more intricate characterization of the spatial *and* temporal scales of the most energetic features of the airwake.

The method begins with arranging CFD (or experimental) velocity data into a 2D matrix as follows [16]

$$D(x,t) = \begin{bmatrix} d(x_1,t_1) & d(x_1,t_2) & \cdots & d(x_1,t_{N_t}) \\ d(x_2,t_1) & d(x_2,t_2) & \cdots & d(x_2,t_{N_t}) \\ \vdots & \vdots & \ddots & \vdots \\ d(x_{N_v \cdot N_s},t_1) & d(x_{N_v \cdot N_s},t_2) & \cdots & d(x_{N_v \cdot N_s},t_{N_t}) \end{bmatrix}, \tag{6}$$

where each quantity d represents a mean-subtracted flow velocity at a given spatial location x and instant in time t. There are N_t time steps (uniform discretization assumed), N_v velocity components and N_s spatial locations. In this work, longitudinal and vertical velocities will be considered individually such that only one velocity component is included in the data matrix D. The order of the spatial discretization as vectors in the data matrix is not exclusive. The procedure of obtaining the vectoral discretization from the physical space should be reversed when interpreting results from the POD [16]. The next step is to take the fast Fourier transform (FFT) in time for each row of the data matrix

$$\widehat{D}(x,\omega) = \text{FFT}\{D(x,t)\} \tag{7}$$

and subsequently compute the cross-spectral density matrix

$$\widehat{K} = \frac{1}{N_t}\widehat{D}^*\widehat{D}, \tag{8}$$

where "*" indicates conjugate transpose. Each element on diagonal of matrix $\widehat{K}$ represents the TKE at given frequency [16]. Half of the values correspond to positive frequency values and the other half to negative frequencies, evident from symmetry in the diagonal values. The TKE values can be plotted to determine the N_{bin} frequency ranges or bins where highly energetic flow features are present. These are readily identified from the peaks in the plot.

The next step is to filter[2] the initial data matrix D from Eq. (6) row by row to generate N_{bin} data matrices, which are then analyzed using POD. The POD formulation diagonalizes the data matrix as follows

[2] In this work, we employ a bandpass filter derived from the one presented in https://tomroelandts.com/articles/how-to-create-simple-band-pass-and-band-reject-filters

$$D = \Phi\Sigma\Psi^{*}, \tag{9}$$

where the columns of Φ contain the orthonormal spatial basis functions, Ψ describes the temporal evolution of the data, and Σ is a diagonal matrix with each entry σ providing a measure of the relative TKE of each spatial mode [16]. The most energetic modes can be identified by plotting the relative TKE contribution α_i of each mode

$$\alpha_i = \frac{\sigma_i}{\sum \sigma_i}. \tag{10}$$

The corresponding spatial modes can then be plotted to identify the primary coherent structures contributing to the TKE. For a more detailed and practical explanation of the POD method, the reader is directed to Ref. [13].

Results

The multi-resolution POD approach was employed for the dynamic characterization of flow features using longitudinal and vertical velocity data aft of the obstacle along the midplanes shown in Figure 4(a) and Figure 4(b). Results for each are presented next.

Dynamic Characterization Along x=0m Plane: Longitudinal Velocity

The midplane shown in Figure 4(a) is considered first, and results are presented for longitudinal velocity. The approach laid out in the previous section was used to determine the cross spectral-density and the TKE associated with each frequency in data. The resulting normalized TKE values are plotted in Figure 17 as a function of Strouhal number (see Eq. (1)). The freestream speed of 30 m/s and cube height of 10m were used as characteristic velocity and length, respectively. The largest peak is noted for the $St \in (0,0.02]$ bin. A bandpass filter was applied to the original data matrix to isolate flow features within this frequency range. The normalized TKE plot obtained from the cross-spectral density matrix of the filtered data is shown in Figure 18, where it is evident that the band-pass filter isolates the frequency bin of interest.

A POD of the filtered data is then performed. The TKE contribution of each mode α_i is plotted in Figure 19. Modes #1 and #2 contribute 58% and 26%, respectively, to the total TKE in that bin. Contour plots of these modes are shown in Figure 20 and Figure 21. From Figure 20, the primary coherent structure in mode #1 is the shear layer that is shed from the top edge of the cube and the associated back step recirculation aft of the cube. Note that flow does not reattach on the top surface of the cube in the simulation considered. The shear layer and aft recirculation contribute to 58% of the TKE associated with flow for $St \in (0,0.02]$. For mode #2, three distinct flow features are noted immediately aft of obstacle in Figure 21: the shear layer between y=10m and y=15m, a recirculation region immediately below it and a secondary recirculation of opposite sign closer to the ground. The second and third features are likely due to the arch vortex aft of the cube and the ground horseshoe vortex, respectively (see Figure 2). The three features contribute to 26% of the TKE associated with flow for $St \in (0,0.02]$.

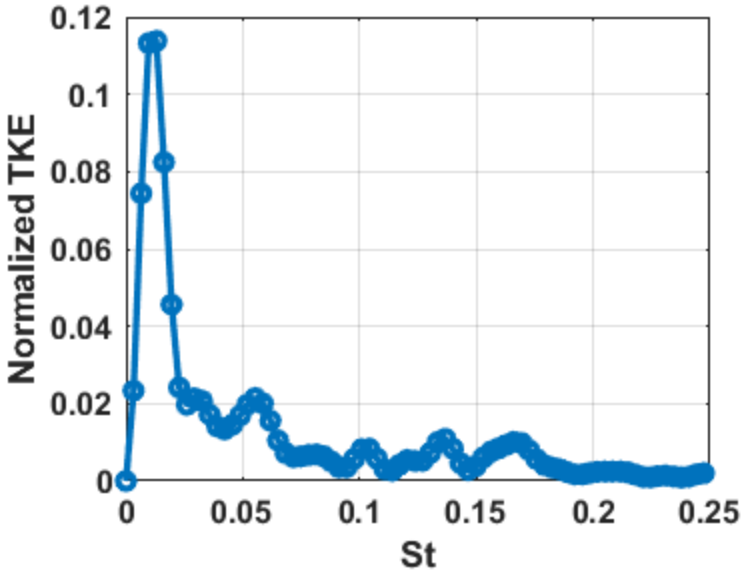

Figure 17: Normalized TKE for longitudinal velocity aft of the obstacle along x=0m plane.

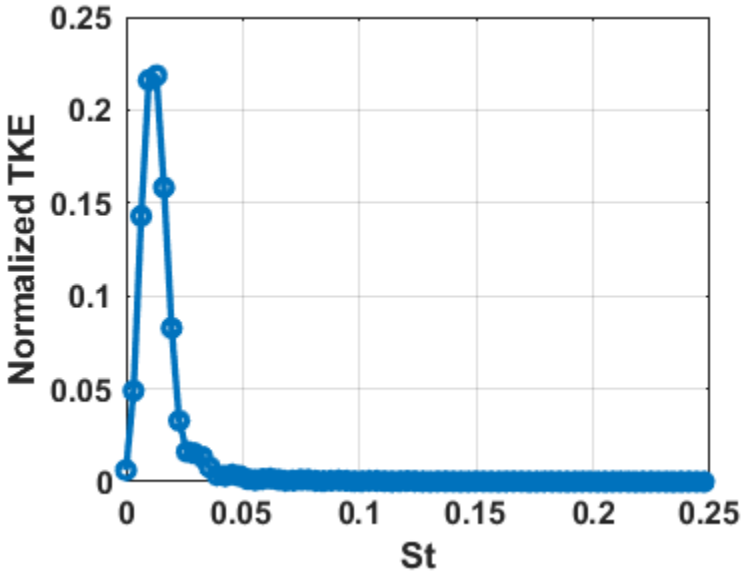

Figure 18: Normalized TKE for filtered longitudinal velocity data aft of the obstacle along x=0m plane.

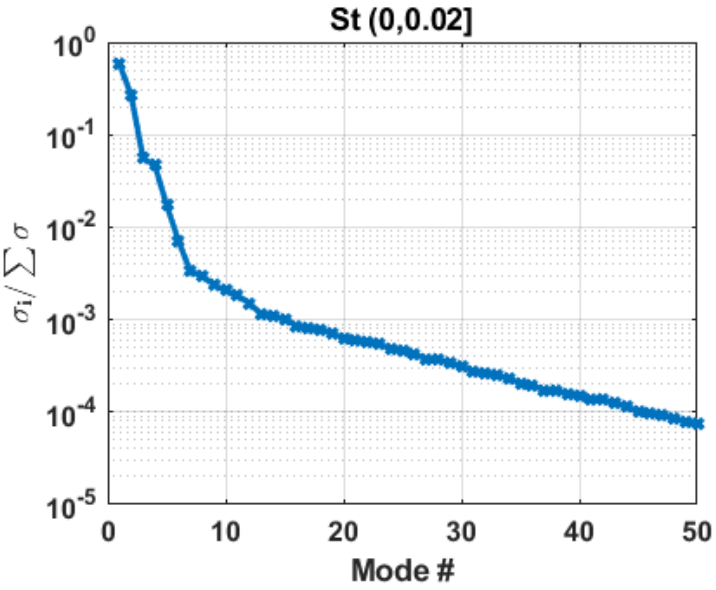

Figure 19: Contribution of each mode to total TKE in $St \in (0,0.02]$ bin; longitudinal velocity aft of the obstacle along x=0m plane considered.

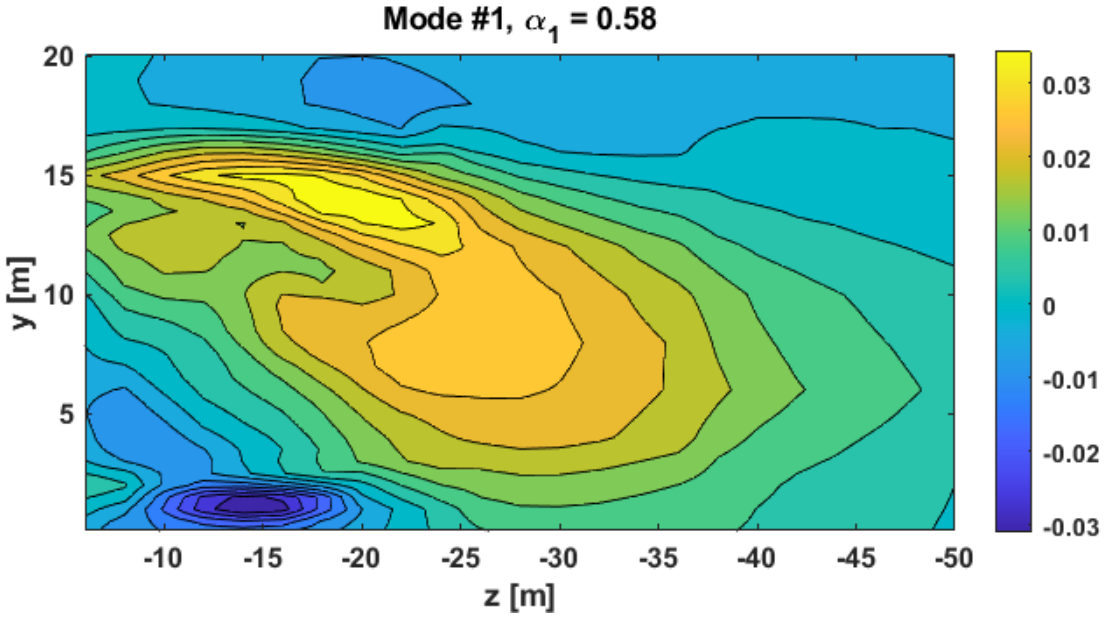

Figure 20: Mode #1 from POD analysis of longitudinal velocity data aft of the obstacle along x=0m plane in $St \in (0,0.02]$ bin.

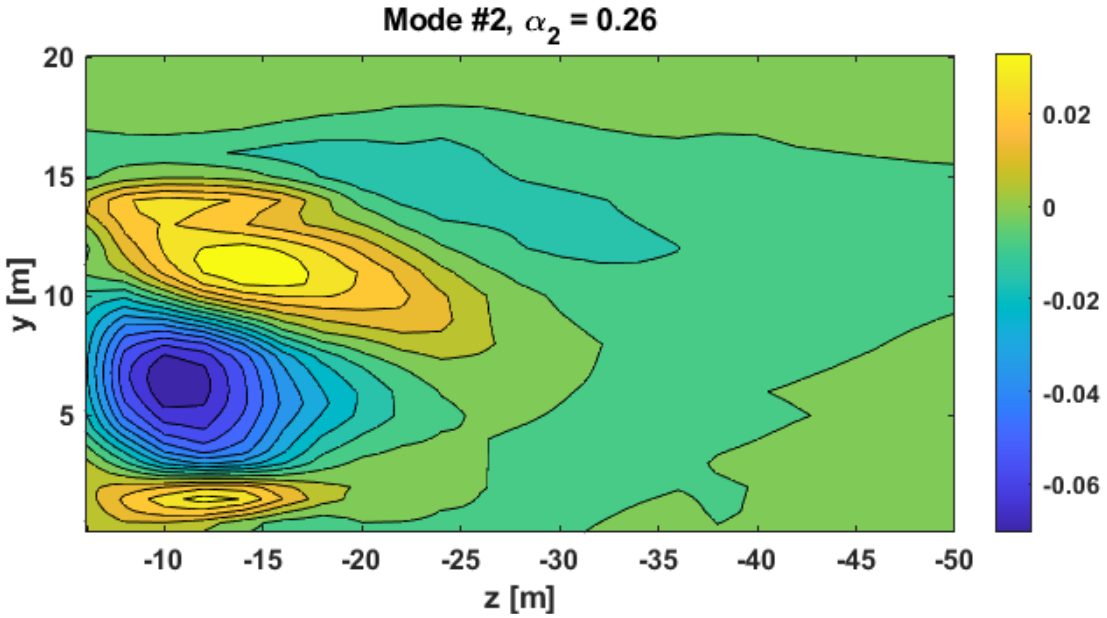

Figure 21: Mode #2 from POD analysis of longitudinal velocity data aft of the obstacle along x=0m plane in $St \in (0,0.02]$ bin.

Dynamic Characterization Along x=0m Plane: Vertical Velocity

The vertical velocity component is particularly important for rotorcraft shipboard operations. The normalized TKE values obtained from the cross-spectral density matrix are plotted in Figure 22. Two frequency bins are identified from the figure: $St \in (0,0.03]$ and $St \in (0.03,0.065]$.

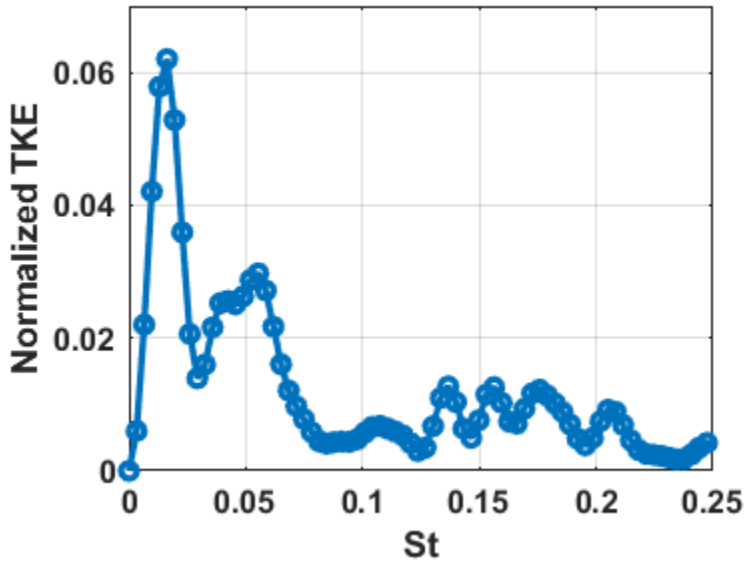

Figure 22: Normalized TKE for vertical velocity aft of the obstacle along x=0m plane.

For the $St \in (0,0.03]$ bin, the first two modes account for 69% of the total TKE. These modes are plotted in Figure 23 and Figure 24. From Figure 23, it is not immediately clear which flow behavior is captured by mode #1. A time lapse of longitudinal velocity contour is shown in Figure 25. From the plots, part of the shear layer gets entrained by freestream while the other get sucked into the recirculation region as time progresses. The contour plot of mode #1 in Figure 23

indicates this flow behavior with the yellow/orange regions indicating part of the shear layer getting entrained by freestream and the blue region indicating the part getting sucked into the aft recirculation. This phenomenon contributes to 36% of the TKE in the $St \in (0,0.03]$ bin. Mode #2, plotted in Figure 24, seems to capture the later stage of the flow entrainment, where the flow associated with the recirculation merges and interacts with the top shear layer. This interaction contributes to 30% of the TKE in the $St \in (0,0.03]$ bin.

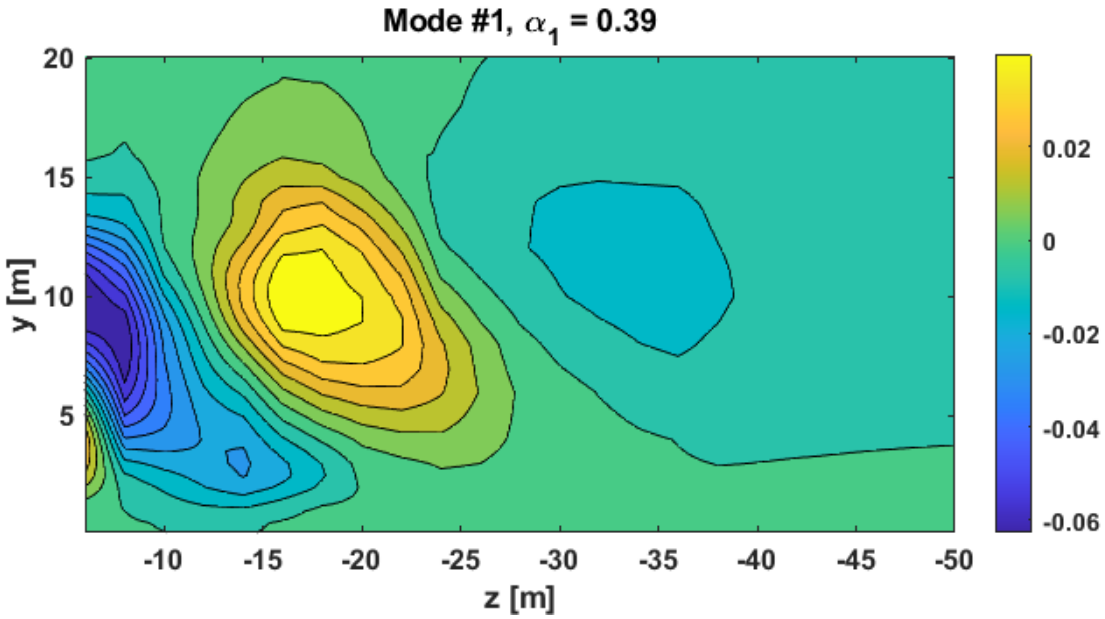

Figure 23: Mode #1 from POD analysis of vertical velocity data aft of the obstacle along x=0m plane in $St \in (0,0.03]$ bin.

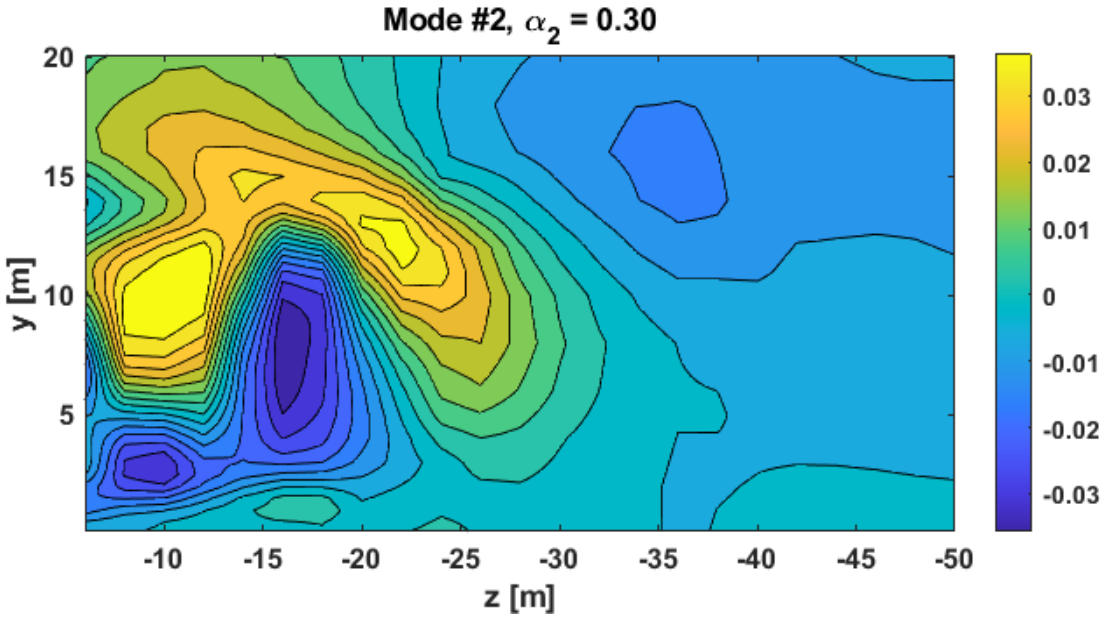

Figure 24: Mode #2 from POD analysis of vertical velocity data aft of the obstacle along x=0m plane in $St \in (0,0.03]$ bin.

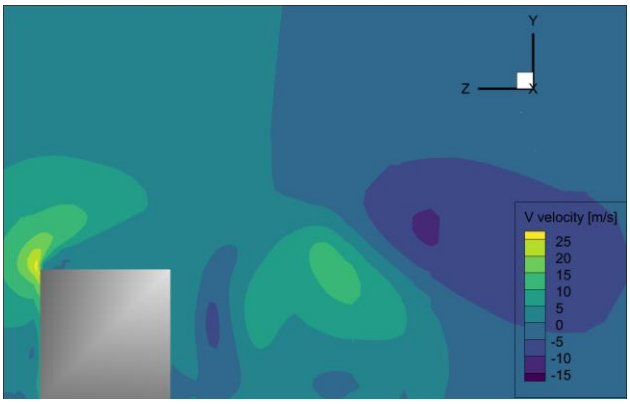

(a) t=5s

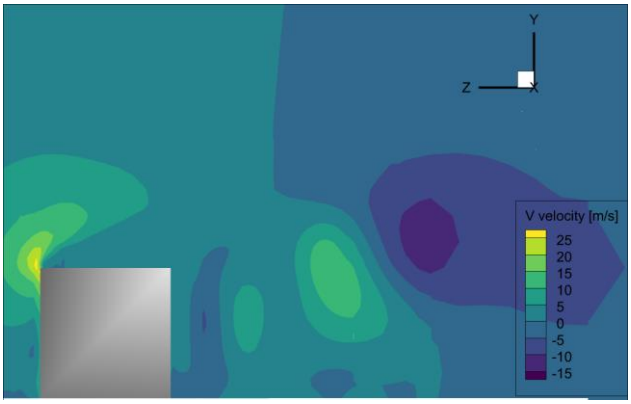

(b) t=5.2s

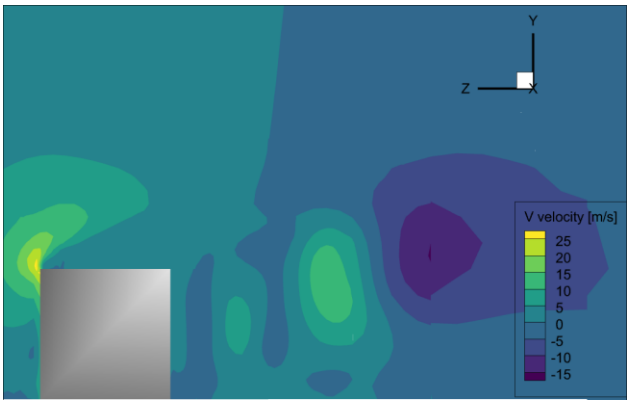

(c) t=5.4s

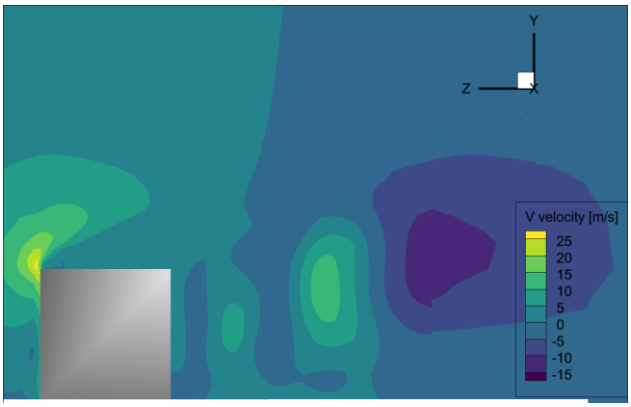

(d) t=5.6s

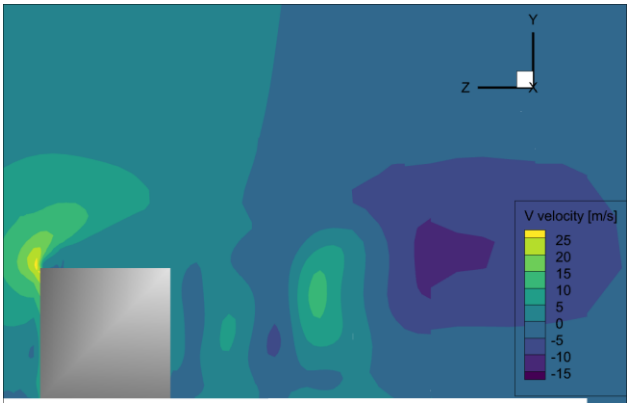

(e) t=5.8s

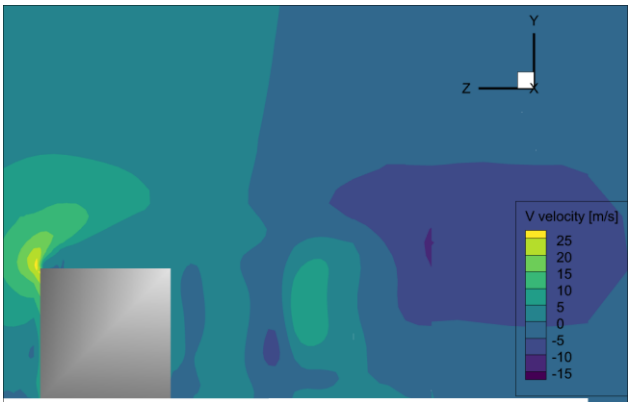

(f) t=6s

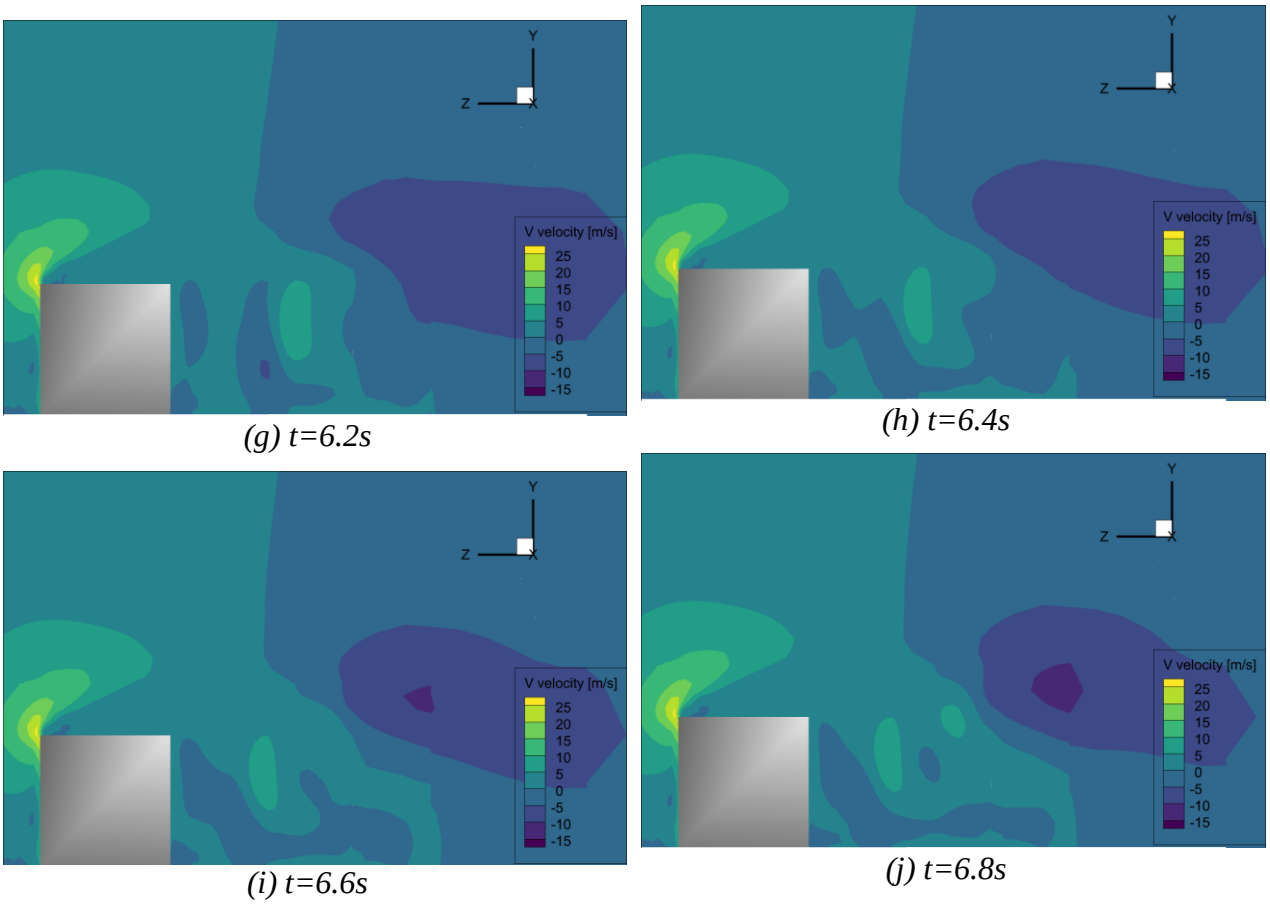

(g) t=6.2s *(h) t=6.4s*

(i) t=6.6s *(j) t=6.8s*

Figure 25: Time-lapse of vertical velocity contour along x=0m plane.

For the $St \in (0.03,0.065]$ bin, it was found mode #1 contributed 36% to the total TKE and exhibited a similar structure to the dominant mode from the previous bin shown in Figure 23. The separation of shear layer flow into parts entrained by freestream and recirculation is thus the most energetic flow phenomena in the combined $St \in (0,0.065]$ range.

Dynamic Characterization Along y=5m Plane: Longitudinal Velocity

The midplane shown in Figure 4(b) is considered in this section. The normalized TKE values obtained using the cross-spectral density matrix from Eq. (8) are shown in Figure 25. The most energetic dynamic flow features occur in the $St \in (0.065,0.1]$ range. A filtered data matrix isolating flow features in this bin was generated and examined using POD. The first two modes contribute the most to the overall TKE in that bin. Mode #1 is plotted in Figure 27. This mode captures the characteristic bistability of flow observed aft of back steps where flow switches intermittently between portside and starboard locations [6,12]. This flow bistability contributes to 38% of the TKE in the $St \in (0.065,0.1]$ bin. Mode #2 displays the onset of the bistability immediately aft of the cube in Figure 28, where the larger alternating flow features seen in mode #1 are broken up into contributions from the shear layer on either side obstacle and associated recirculation regions. Mode #2 contributes to 27% of the TKE in the $St \in (0.065,0.1]$ bin. Note that Zhu et al. [6] identify the bistable flow feature in the $St \in (0, 0.06]$ bin in their experimental study, which considered three headwinds (15.2, 45.7 and 61 m/s) over 1/90th scale model of the

SFS2 ship geometry. The discrepancy between their results and ours is potentially due to the inclusion of a simulated ABL in the experiments.

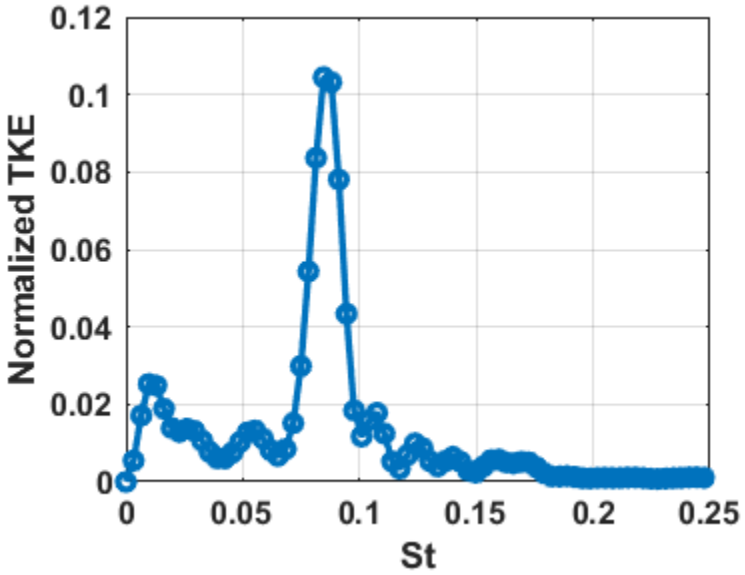

Figure 26: Normalized TKE for longitudinal velocity aft of the obstacle along y=5m plane.

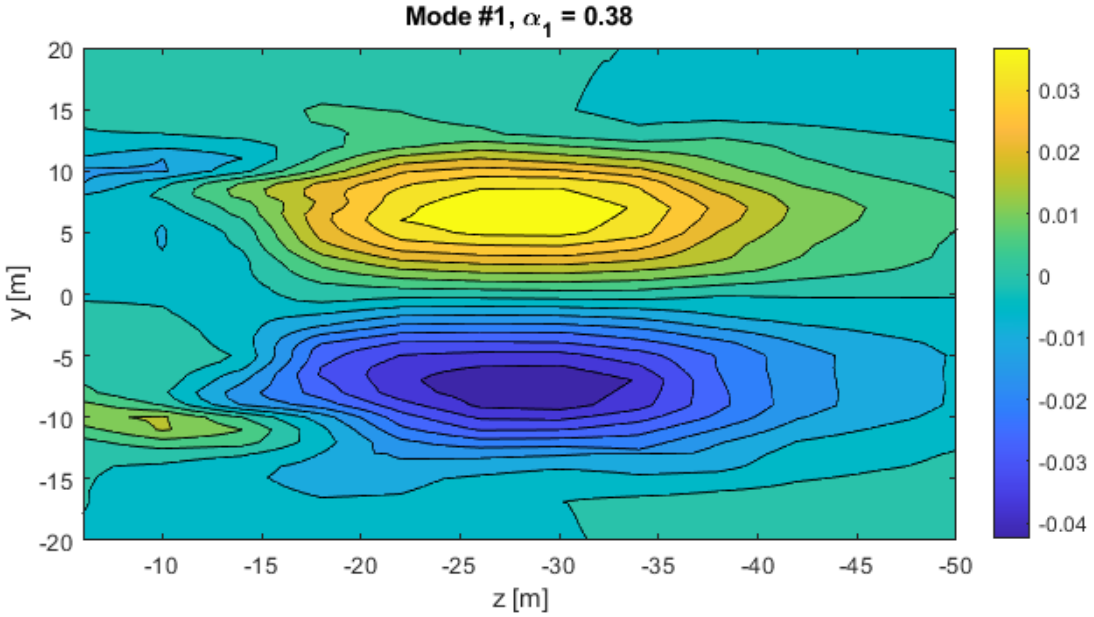

Figure 27: Mode #1 from POD analysis of longitudinal velocity data aft of the obstacle along y=5m plane in $St \in (0{,}065, 0.1]$ bin.

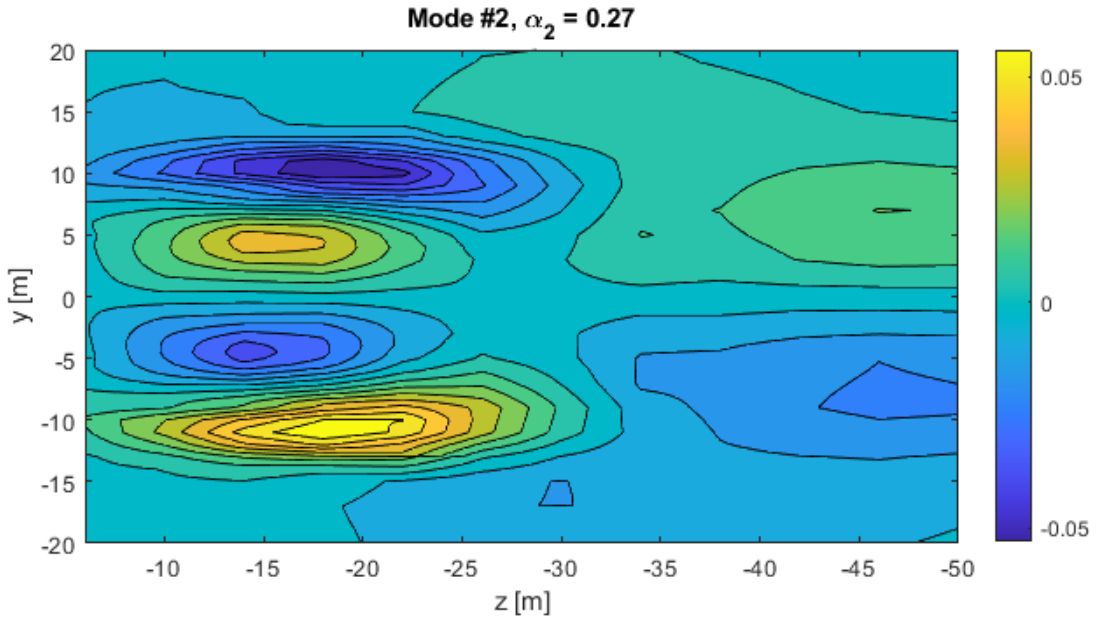

Figure 28: Mode #2 from POD analysis of longitudinal velocity data aft of the obstacle along y=5m plane in $St \in (0{,}065, 0.1]$ bin.

Dynamic Characterization Along y=5m Plane: Veritcal Velocity

For the vertical velocity, the same frequency bin of $St \in (0.065,0.1]$ and bistable flow feature are identified. Results are not shown here for brevity.

It is important to note that the energetic flow features identified in the results above are all present in low frequency bins that can directly influence aircraft flight dynamics and handling qualities.

Discussion

Airwake velocities can be broken down into mean and fluctuating components. The analytical models described in the time-averaged characterization section provide a way to quantify the length scales of coherent flow structures. By supplementing this information with time scale and qualitative flow feature characterization information from the dynamic characterization section, a thorough spatiotemporal characterization of energetic flow features that influence aircraft flight dynamics and handling qualities can be obtained. During the upcoming reporting period, we plan to finalize the time-averaged model fitting for vertical velocity and perform further dynamic characterization of primary flow features (notably for deck-edge vortices). We also plan to further explore parametrization and scaling of the characterization in terms of obstacle dimensions, wind speed and direction.

Plans for the Next Reporting Period

In the next reporting period, we will build upon the understanding of the types of flowfields experienced by naval aviators described above and continue to quantify the scales and nature of the relevant primary flow structures based on the ongoing CFD predictions. Development of representative "canonical" surrogate flowfields will continue. Work will commence on the helicopter flight dynamic simulations, and we will start the request/approval process for the CASTLE V-22 tiltrotor model.

References

1. Smith, M.J., et al. *Identification and Quantification of the Role of Turbulence in Aircraft/Ship Aerodynamics*. *ONR Annual Review*. 2020. Arlingon, VA.
2. Silva, M.J., et al. *The Role of Modeling & Simulation in the Mitigation of V-22 Tiltrotor Formation Flight Wake-Induced Roll-off. 72nd Annual Forum of the American Helicopter Society*. 2016. West Palm Beach, FL.
3. Whitehouse, G.R. and R.E. Brown. *Modelling a Helicopter Rotor's Response to Encounters with Aircraft Wakes*. in *28th European Rotorcraft Forum*. 2002. Bristol, UK.
4. Whitehouse, G.R. and R.E. Brown. *Helicopter Rotor Response to Wake Encounters in Ground Effect*. in *59th Annual Forum of the American Helicopter Society*. 2003. Phoenix, AZ.
5. Whitehouse, G.R. and R.E. Brown, *Modelling the Mutual Distortions of Interacting Helicopter and Aircraft Wakes.* Journal of Aircraft, 2003. **Vol. 40**(No. 3): p. pp. 440-449.
6. Whitehouse, G.R. and R.E. Brown, *Modelling a Helicopter Rotor's Response to Wake Encounters.* The Aeronautical Journal, 2004. **Vol. 108**(No. 1079): p. pp. 15-26.
7. Whitehouse, G.R., *Helicopter Response to Vortex Encounters in the Near-Airfield Environment*, 2003, PhD Thesis, Department of Aeronautics Imperial College London.
8. ADS-33E-PRF. *Aeronautical Design Standard Performance Specification Handling Qualities Requirements for Military Rotorcraft*. in *US Army Aviation and Missile Command, Aviation Engineering Directorate*. 2000. Redstone Arsenal, Alabama.
9. Banks, D. and R.N. Meroney, *A Model of Roof-Top Surface Pressures Produced by Conical Vortices: Evaluation and Implications.* Wind and Structures, 2001. **Vol. 4**(No. 3): p. pp. 279–298.
10. Yakhot, A., et al., *Turbulent Flow Around a Wall-Mounted Cube: A Direct Numerical Simulation.* International Journal of Heat and Fluid Flow, 2006. **Vol. 27**(No. 6): p. pp. 994-1009.
11. Klotz, L., et al., *Experimental Investigation of Flow Behind a Cube for Moderate Reynolds Numbers.* Journal of Fluid Mechanics, 2014. **Vol. 750**: p. pp. 73–98.
12. Banks, D. and R.N. Meroney, *A Model of Roof-Top Surface Pressures Produced by Conical Vortices: Model Development.* Wind and Structures, 2001. **Vol. 4**(No. 3): p. pp. 227–246.
13. Weiss, J. *A Tutorial on the Proper Orthogonal Decomposition*. *AIAA Aviation 2019 Forum*. 2019. Dallas, TX: AIAA-2019-3333.
14. Schmidt, O.T. and T. Colonius, *Guide to Spectral Proper Orthogonal Decomposition.* Journal of Aircraft, 2020. **Vol. 58**(No. 3).
15. Mendez, M.A., et al., *Multi-Scale Proper Orthogonal Decomposition of Complex Fluid Flows.* Journal of Fluid Mechanics, 2019. **Vol. 870**.
16. Zhu, N., et al. *Dynamics of Large-Scale Flow Structures Within Ship Airwakes*. *AIAA SCITECH 2022 Forum*. 2022. San Diego, CA: AIAA-2022-2532.
17. Li, C.Y., et al., *Dynamic Mode Decomposition on Pressure Flow Field Analysis: Flow Field Reconstruction, Accuracy, and Practical Significance.* Journal of Wind Engineering and Industrial Aerodynamics, 2020. **Vol. 205**.
18. Schmid, P.J., *Dynamic Mode Decomposition of Numerical and Experimental Data.* Journal of Fluid Mechanics, 2010. **Vol. 656**.
19. Tu, J.H., et al., *On Dynamic Mode Decomposition: Theory and Applications.* Journal of Computational Dynamics, 2014. **Vol. 1**(No. 2).

20. Tu, J.H., *Dynamic Mode Decomposition: Theory and Applications*, in *PhD, Department of Mechanical and Aerospace Engineering* 2013, Princeton University.
21. Kim, K.C., et al., *Flow Structure around a 3-D Rectangular Prism in a Turbulent Boundary Layer.* Journal of Wind Engineering and Industrial Aerodynamics, 2003. **Vol. 91**(No. 5): p. pp. 653-669.